© 2026. Published by The Company of Biologists | Journal of Cell Science (2026) 139, jcs264804. doi:10.1242/jcs.264804

RESEARCH ARTICLE

The molecular composition of JRAB/MICAL-L2 droplets controls site-specific actin bundle morphology to drive cell–cell adhesion

Ayuko Sakane[1,2,*], Christian Ganser[3], Kazuki Horikawa[4], Chie Sakamoto[1], Mayu Sakai[1], Maho Okada[1], Nodoka Ono[1], Natsuki Matsushita[5], Hiroshi Yamada[6], Kohji Takei[6], Kou Motani[7], Yosuke Matsushita[8], Toyomasa Katagiri[8], Kaoru Katoh[9,10,11], Hiroshi Kawabe[12], Shigenobu Yonemura[13], Takayuki Uchihashi[3,14] and Takuya Sasaki[15]

ABSTRACT

JRAB (also known as MICAL-L2), an effector protein for the small G proteins Rab8A and Rab13, interacts with actin filaments (F-actin), actinin-1, actinin-4 and filaminA, and plays an important role in the spatiotemporal actin cytoskeletal reorganization underlying cell migration and cell–cell adhesion. JRAB forms droplets that include Rab8A by liquid–liquid phase separation, leading to deformation of the endosomal membrane. In this study, we showed that JRAB functions in actin dynamics as a droplet, leading to the development of cell–cell adhesions. *In vitro* reconstitution assays revealed that JRAB droplets promoted the assembly of thick F-actin bundles, a process that was distinct from that observed with JRAB in its soluble form. Moreover, we identified Rab13 as a modulator of JRAB droplet function. JRAB droplets containing Rab13 inhibited the formation of F-actin bundles. The difference in mechanical properties among those droplets might be correlated with the ability of JRAB to regulate F-actin bundle morphology. Taken together, our findings provide new insight into a previously unrecognized mechanism through which droplets regulate actin dynamics by changing their components.

[1]Molecular and Cellular Function Unit, Institutes of Photonics and Human Health Frontier, Tokushima University, Tokushima 770-8503, Japan. [2]Department of Interdisciplinary Researches for Medicine and Photonics, Institute of Post-LED Photonics, Tokushima 770-8503, Japan. [3]Department of Creative Research, Exploratory Research Center on Life and Living Systems, National Institutes of Natural Sciences, Okazaki 444-8787, Japan. [4]Department of Optical Imaging, Tokushima University Graduate School of Medicine, Tokushima 770-8503, Japan. [5]Division of Laboratory Animal Research, Aichi Medical University School of Medicine, Nagakute 480-1195, Japan. [6]Department of Neuroscience, Okayama University Graduate School of Medicine, Dentistry and Pharmaceutical Sciences, Okayama 700-8558, Japan. [7]Division of Cell Signaling, Fujii Memorial Institute of Medical Sciences, Institute of Advanced Medical Sciences, Tokushima University, Tokushima 770-8503, Japan. [8]Laboratory of Biofunctional Molecular Medicine, National Institute of Biomedical Innovation, National Institutes of Biomedical Innovation, Health and Nutrition, Osaka 567-0085, Japan. [9]Exploratory Research Center on Life and Living Systems, National Institutes of Natural Sciences, Okazaki 444-8787, Japan. [10]Artificial Intelligence Research Center, National Institute of Advanced Industrial Science and Technology, Tokyo 135-0064, Japan. [11]Ph.D. Program in Humanics, School of Integrative and Global Majors, University of Tsukuba, Tsukuba 305-8577, Japan. [12]Department of Pharmacology, Gunma University Graduate School of Medicine, Maebashi 371-8511, Japan. [13]Department of Cell Biology, Tokushima University Graduate School of Medicine, Tokushima 770-8503, Japan. [14]Department of Physics and Structural Biology Research Center, Nagoya University, Nagoya 464-8602, Japan. [15]J-PEAKS Program Office, Tokushima University, Tokushima 770-8503, Japan.

*Author for correspondence (sakane@tokushima-u.ac.jp)

A.S., 0000-0002-7454-2887

This is an Open Access article distributed under the terms of the Creative Commons Attribution License (https://creativecommons.org/licenses/by/4.0), which permits unrestricted use, distribution and reproduction in any medium provided that the original work is properly attributed.

Handling Editor: Michael Way
Received 17 February 2026; Accepted 17 September 2026

KEY WORDS: Liquid–liquid phase separation, JRAB, MICAL-L2, Rab13, Actin bundle morphology, Cell–cell adhesion

INTRODUCTION

Small G proteins of the Rab family are involved in the regulation of membrane trafficking (Hutagalung and Novick, 2011; Stenmark, 2009; Wandinger-Ness and Zerial, 2014; Zerial and McBride, 2001; Zhen and Stenmark, 2015). In mammalian cells, the Rab family consists of more than 70 members. Each Rab protein is located on a distinct organelle membrane or the plasma membrane, where it subsequently regulates the transport of proteins or lipids. Each Rab protein can interchange between its GTP-bound active form and GDP-bound inactive form. GTP-bound Rab interacts with specific proteins, called effector proteins, and the Rab–effector protein complex provides each Rab with a specific function (Grosshans et al., 2006). Thus, when determining the cellular function of a Rab protein, its effector protein must first be identified.

The MICAL family consists of MICAL proteins and MICAL-like proteins (Giridharan and Caplan, 2014). Members of the MICAL family have been well characterized as regulators of the actin cytoskeleton (Giridharan and Caplan, 2014; Giridharan et al., 2012). Canonical MICAL proteins, such as MICAL1, function as flavoprotein monooxygenases that promote actin filament (F-actin) disassembly through redox-dependent mechanisms (Hung et al., 2011; Zucchini et al., 2011). In contrast, JRAB (also known as MICAL-L2), a MICAL-like protein, lacks the monooxygenase domain and regulates the actin cytoskeleton through mechanisms distinct from MICAL1 (Miyake et al., 2019; Nakatsuji et al., 2008; Sakane et al., 2012, 2013; Terai et al., 2006).

MICAL and MICAL-like proteins have been shown to functionally interact with Rab proteins (Giridharan and Caplan, 2014). Among these, JRAB functions as an effector protein of Rab13 (Terai et al., 2006; Yamamura et al., 2008). The JRAB–Rab13 complex contributes to cell adhesion through the transport of cell adhesion molecules to the plasma membrane (Sakane and Sasaki, 2015; Terai et al., 2006; Yamamura et al., 2008). Additionally, JRAB interacts with F-actin and localizes to the thick F-actin bundles along the cell-free border (Sakane et al., 2012). JRAB at cell–cell contacts might associate with the thinner F-actin structures that reinforce cell–cell adhesions (Sakane et al., 2012).

These observations led us to speculate that JRAB plays multiple roles in the spatiotemporal rearrangement of F-actin bundles during collective cell migration (Sakane et al., 2016). However, the underlying mechanisms that generate distinct actin architectures at the cell-free border and at cell–cell adhesion sites remain unclear.

Recently, JRAB has been shown to localize to the recycling endosomal membrane, one of the organelles involved in the recycling pathway of intracellular vesicle trafficking, through

Journal of Cell Science (2026) 139, jcs264804. doi:10.1242/jcs.264804

interaction with Rab8A to form the long, elongated tube structure required for the function of recycling endosomes (Sakane et al., 2021). Furthermore, JRAB forms droplets by liquid–liquid phase separation (LLPS), and Rab8A-containing droplets of JRAB induce the membrane deformation of recycling endosomes.

In this study, we show that JRAB droplets are involved in the regulation of F-actin bundle morphology (thickness and length) along the cell-free border and cell–cell contact regions. Our *in vitro* experiments revealed that Rab13 is recruited to JRAB droplets and that these droplets inhibit the formation of F-actin bundles. Moreover, we show that JRAB droplets containing Rab13 are irregular and stiffer than JRAB droplets without Rab13. Furthermore, we find that the incorporation of Rab13 restricts the mobility of JRAB within the droplet, thereby limiting its availability for transfer onto F-actin bundles. These results suggest that the difference in mechanical properties among the droplets is correlated with the function of JRAB in the formation of thick F-actin bundles. Taken together, our findings show that JRAB functions as a droplet and is regulated by Rab13, providing new insight into actin organization and dynamics.

RESULTS

JRAB regulates actin filaments along the free border and at cell–cell adhesion sites of epithelial cells

To investigate the role of JRAB in the regulation of the actin cytoskeleton, we generated JRAB-knockout (KO) MTD-1A cells using CRISPR-Cas9 technology. The KO of JRAB in the cells was confirmed by western blot analysis using anti-GAPDH and anti-JRAB antibodies (Fig. 1A). In the KO cells (designated KO-1 and KO-2 for two different clones), the F-actin bundles at the leading edge were looser than those in the control cells (Fig. 1Ba, arrowheads, Bb). This finding is consistent with our previous results from the siRNA-mediated knockdown of JRAB (Sakane et al., 2012). In addition, the actin fibers just beneath cell–cell adhesion sites were disordered, with disrupted fiber orientation and loosening of the F-actin bundles in the KO cells (Fig. 1Ba, arrows). To determine whether the actin cytoskeletal abnormalities observed at the cell-free edge and at cell–cell adhesions in the KO cells are truly attributable to the loss of JRAB, we generated cells in which GFP–JRAB was re-expressed in the JRAB-KO background (Fig. S1A). In these cells, the actin cytoskeletal abnormalities observed in the KO cells were completely reversed, as demonstrated by phalloidin staining (Fig. S1B).

Thin F-actin bundles extend radially from near the thick F-actin bundle at the cell-free edge toward the extracellular matrix, where they form focal adhesions (FAs) (Sakane et al., 2012, 2016). The FA is the cell–matrix adhesion structure and generates traction force (Balaban et al., 2001; Zaidel-Bar et al., 2003). We therefore examined the role of JRAB in the formation of FAs by immunostaining with an antibody against vinculin, which is a FA protein. In control cells, long vinculin-positive structures were frequently observed at the free edge (Fig. 1Ca, arrows), whereas the KO cells predominantly exhibited shorter, punctate vinculin-positive structures (Fig. 1Ca, dots). The long and short vinculin-positive structures correspond to mature and immature FAs, respectively (Pasapera et al., 2010; Zaidel-Bar et al., 2003). To quantitatively evaluate FA maturation, we measured the Feret diameter of individual vinculin-positive FAs. The cumulative distribution of FA length was shifted toward longer FAs in the control cells compared with two independent KO cell lines, indicating enhanced FA maturation (Fig. 1Cb). Consistent with this observation, the proportion of long FAs (Feret diameter >2 µm) was significantly higher in the control cells than in the two independent KO cell lines (Fig. 1Cc). Furthermore, experiment-level analysis demonstrated that the mean FA length was significantly greater in the control cells than in either KO cell line (Fig. 1Cd).

Because FA maturation involves dynamic assembly and disassembly, we next examined FA dynamics using control and KO-1 cells stably expressing GFP–paxillin. GFP–paxillin-positive FAs were tracked by live-cell imaging (Movie 1), and FA lifetime, assembly rate and disassembly rate were quantified from changes in GFP–paxillin fluorescence intensity over time. FA lifetime and assembly rate were not significantly different between control and KO-1 cells (Fig. S1Ca,b), whereas the disassembly rate was significantly higher in KO-1 cells (Fig. S1Cc). These results suggest that loss of JRAB alters FA dynamics, with the most evident effect on FA disassembly. Together with the reduced formation of mature FAs observed by vinculin staining, these results suggest that JRAB promotes the formation of thick F-actin bundles, which in turn supports FA maturation and stability. Consistent with this, re-expression of GFP–JRAB rescued the defect in FA maturation, as assessed by vinculin staining (Fig. S1B).

JRAB regulates cell–cell adhesion through actin cytoskeletal reorganization just beneath the cell–cell contact site

Next, we examined the role of JRAB in maintaining cell–cell adhesion. Tight junctions (TJs) maintain cell–cell adhesion and regulate the barrier function of epithelial cells (Tsukita et al., 2001). Claudins are a family of integral membrane proteins that are essential components of TJs in epithelial cells. At least 27 claudin members have been identified in humans (Furuse and Tsukita, 2006; Tsukita et al., 2019). Our RNA-seq data revealed that claudin-4 was the most highly expressed claudin in MTD-1A cells (Table S1). In control cells, claudin-4 was aligned at cell–cell contact sites, whereas in KO cells, it did not localize linearly at cell–cell adhesion sites (Fig. 2A). Moreover, we examined ZO-1, which is also a TJ protein, which connects claudins to the actin cytoskeleton (Itoh et al., 1999; Stevenson et al., 1986). In control cells, ZO-1 was aligned at cell–cell contact sites, whereas in KO cells, the localization was disrupted, as ZO-1 no longer formed a continuous linear pattern at cell–cell junctions but instead appeared discontinuous (Fig. 2B). This is probably due to the disordered F-actin just beneath the cell–cell adhesion site.

We also examined the effect of JRAB KO on the maintenance of adherens junctions (AJs), another cell–cell adhesion structure. E-cadherin is a main component of AJs (Hartsock and Nelson, 2008). α-Catenin, another AJ protein, associates with F-actin (Pokutta and Weis, 2002). In the KO cells, E-cadherin and α-catenin did not localize linearly at cell–cell adhesion sites, appeared discontinuous, and exhibited a wavy and punctate staining pattern (Fig. 2C,D). Re-expression of GFP–JRAB significantly decreased the junctional discontinuity index and restored continuous cell–cell junctions positive for claudin-4, ZO-1 (also known as TJP1), E-cadherin and α-catenin (Fig. S1D). These results indicate that JRAB regulates cell–cell adhesion through actin cytoskeletal reorganization just beneath the cell–cell contact site.

Latrunculin A induces the formation of droplet-like structures containing JRAB in epithelial cells

To determine the relationship between JRAB and F-actin dynamics (construction and collapse) inside the cells, we treated cells expressing GFP–JRAB with latrunculin A (LatA), an inhibitor of actin polymerization, to disrupt F-actin structures (Spector et al., 1983). Upon LatA treatment, F-actin at the free edge and cell–cell

Journal of Cell Science (2026) 139, jcs264804. doi:10.1242/jcs.264804

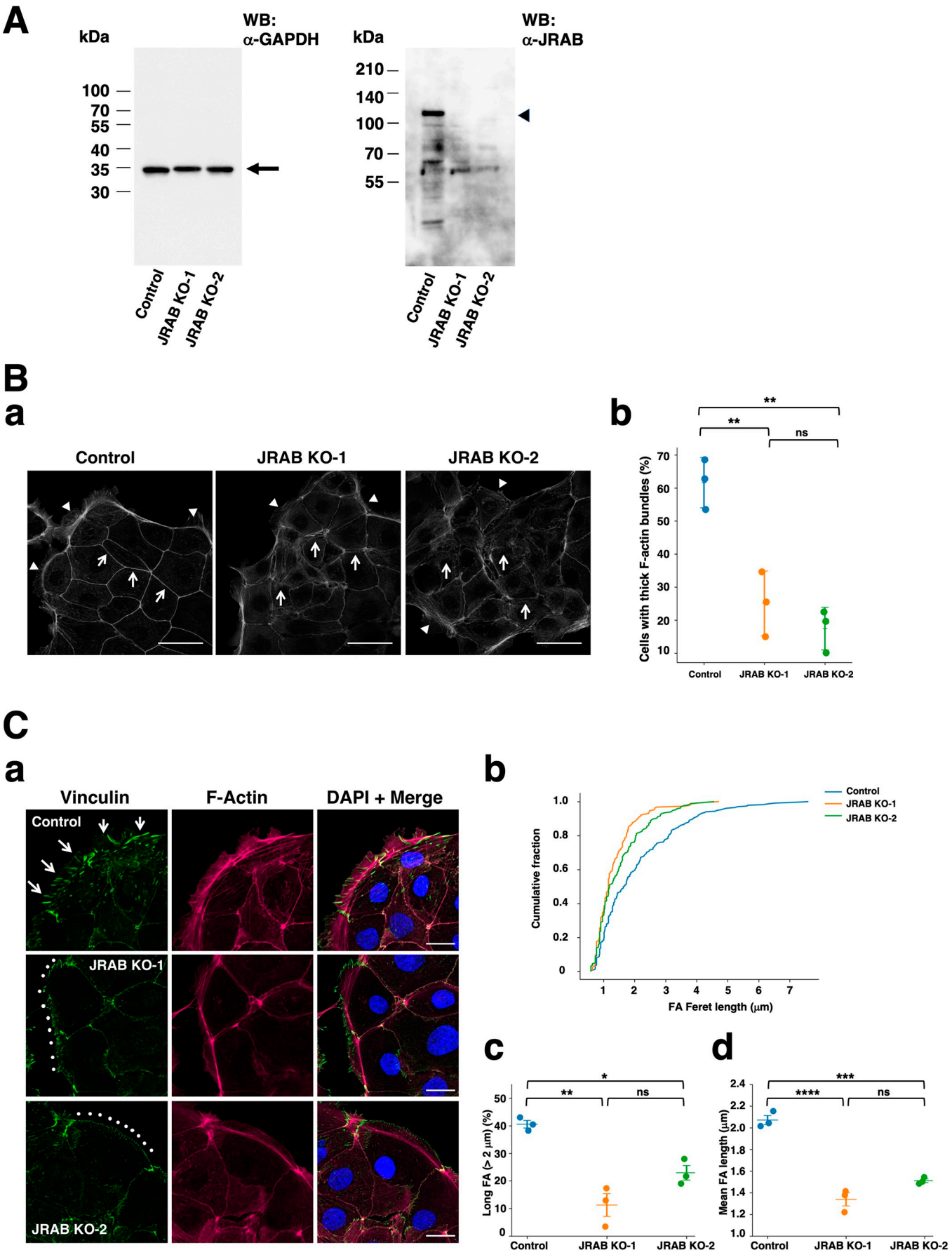


Fig. 1. See next page for legend.

Journal of Cell Science

Journal of Cell Science (2026) 139, jcs264804. doi:10.1242/jcs.264804

Fig. 1. Establishment and characterization of JRAB knockout (KO) MTD-1A cells. (A) JRAB KO was confirmed by western blotting (arrowhead). GAPDH was used as a loading control (arrow). The experiments were repeated independently three times with similar results. (B) (a) Effect of JRAB KO on actin filaments at the free border and cell–cell adhesion sites of MTD-1A cells. Control cells and two independent JRAB KO cell lines (JRAB KO-1 and KO-2) were stained with rhodamine–phalloidin. Representative images from three independent experiments are shown. Arrowheads indicate actin filaments at the free border; arrows indicate actin filaments at cell–cell adhesion sites. Scale bars: 50 µm. (b) The percentage of cells exhibiting thick F-actin bundles along the free border was quantified. A total of 121, 139 and 155 control, JRAB KO-1, and KO-2 cells, respectively, from three independent experiments were analyzed. Each dot represents one independent experiment (n=3). Bars indicate mean±s.d. **P<0.01; ns, not significant (one-way ANOVA followed by Tukey's multiple comparisons test; control versus JRAB KO-1, P=0.004; control versus JRAB KO-2, P=0.001; JRAB KO-1 versus JRAB KO-2, P=0.520). (C) (a) Effect of JRAB KO on focal adhesion formation. Control, JRAB KO-1 and KO-2 cells were stained with an anti-vinculin antibody to visualize focal adhesions. F-actin and nuclei were visualized with rhodamine–phalloidin (magenta) and DAPI (blue), respectively. Representative images from three independent experiments are shown. Arrows indicate mature focal adhesions; dots indicate immature focal adhesions. Scale bars: 20 µm. (b) Cumulative distribution of focal adhesion Feret diameter measured from all detected focal adhesions. Each curve represents pooled object-level measurements from three independent experiments. The distribution in the control cells is shifted toward longer focal adhesions compared with JRAB KO-1 and KO-2 cells. (c) Percentage of long focal adhesions (Feret diameter>2 µm). For each independent experiment, the percentage of focal adhesions with a Feret diameter>2 µm was calculated. Each dot represents one independent experiment (n=3). Bars indicate mean±s.e.m. *P<0.05; **P<0.01; ns, not significant (one-way ANOVA followed by Tukey's multiple-comparisons test; control versus JRAB KO-1, P=0.0010; control versus JRAB KO-2, P=0.0126; JRAB KO-1 versus JRAB KO-2, P=0.0682). (d) Mean focal adhesion length. The mean Feret diameter of vinculin-positive focal adhesions was calculated for each independent experiment. Each dot represents one independent experiment (n=3). Bars indicate mean±s.e.m. ***P<0.001; ****P<0.0001; ns, not significant (one-way ANOVA followed by Tukey's multiple-comparisons test; control versus JRAB KO-1, P<0.0001; control versus JRAB KO-2, P=0.0002; JRAB KO-1 versus JRAB KO-2, P=0.0682).

adhesion sites disassembled, accompanied by the time-dependent appearance of GFP–JRAB droplet-like structures in the cytoplasm (Fig. 3Aa; Movie 2). Quantitative analysis showed a progressive increase in both the number and size of GFP–JRAB droplets following LatA treatment (Fig. 3Ab,c). In contrast, GFP alone did not form droplet-like structures (Fig. S2).

Importantly, endogenous JRAB also formed similar droplet-like structures following LatA treatment (upper panels in Fig. S3). In untreated cells, endogenous JRAB localized to thick F-actin bundles at the free edges and thin F-actin bundles underlying cell–cell adhesions, consistent with the localization of exogenous GFP–JRAB (lower panels in Fig. S3). These observations indicate that LatA-induced droplet formation is not restricted to exogenously expressed GFP–JRAB.

We have previously reported that JRAB undergoes LLPS and that recombinant GFP–JRAB protein forms liquid-like droplets in the presence of the crowding agent polyethylene glycol (PEG) *in vitro* (Sakane et al., 2021). We therefore examined whether the LatA-induced GFP–JRAB droplets were sensitive to 1,6-hexanediol (1,6-HD), a reagent commonly used to assess the contribution of weak hydrophobic interactions to the formation of biomolecular condensates (Kroschwald et al., 2017). Treatment with 1,6-HD significantly reduced both the area occupied by GFP–JRAB droplets and their average size (Fig. 3Ba–c), further supporting their liquid-like nature.

We next examined whether LatA-induced droplet formation was reversible. Upon LatA washout, GFP–JRAB droplets disappeared, followed by the reformation of cell–cell adhesions and thick F-actin bundles at the free edge (Fig. S4; Movie 3).

Finally, we analyzed the ultrastructure of GFP–JRAB droplet-like structures identified by confocal microscopy using correlative light and electron microscopy (CLEM) (Fig. 3C). The CLEM images revealed that the fluorescence signal of GFP–JRAB droplet corresponded to an amorphous, electron-dense region that appeared distinct from the surrounding cytoplasm (Fig. 3Cd–g). Within these regions, ribosomes and membranous organelles were rarely observed (Fig. 3Cd–g). These observations suggest that LatA induces GFP–JRAB droplet-like assemblies with ultrastructural features different from the bulk cytoplasm, although further quantitative and high-resolution analyses will be required to fully characterize their properties.

Next, we investigated whether JRAB droplets could be observed in the epithelial cells even in the absence of LatA. Accordingly, the localization of GFP–JRAB at the inside of the bundle was closely examined by super-resolved three-dimensional stimulated emission depletion microscopy (3D-STED) (Fig. S5A,B). The droplet-like structures of GFP–JRAB localized apart from F-actin in the cytoplasm (arrows). We speculated that the JRAB droplets that were not bound to F-actin provide a JRAB reservoir for its regulation of F-actin bundles along the free borders or cell–cell adhesion sites. These results suggest that JRAB droplets might be constitutively present under physiological conditions, that is, in the absence of LatA.

JRAB droplets regulate actin filaments at the free borders and cell–cell adhesion sites of epithelial cells

Using the JRAB KO cells described above, we found that JRAB was involved in the regulation of F-actin bundle morphology at the cell-free border and cell–cell adhesion sites. Moreover, we closely examined the localization of GFP–JRAB in regions where F-actin bundles formed by 3D-STED (Fig. S5A,C). Small clusters of GFP–JRAB localized on the surface of the small bundle of F-actin (arrows), and condensed GFP–JRAB appeared to connect several small bundles of F-actin, leading to the formation of thick bundles (arrowheads).

Based on these results, we next investigated whether the JRAB 'droplets' are involved in the process of F-actin bundle formation. GFP–JRAB-expressing cells were treated with LatA-containing medium for 60 min, followed by incubation in fresh medium for 5 min. The medium was then replaced with fresh medium, and the cells were fixed 30 or 60 min later (timeline at the top of Fig. 4). During this period, F-actin bundles gradually developed along cell-free edges and at cell–cell contact sites over time (upper panels in Fig. 4A,Ba). To examine the effect of disrupting JRAB droplets, cells were treated with LatA for 60 min, followed by incubation in fresh medium containing 1,6-HD for 5 min. The medium was then replaced with fresh medium, and the cells were fixed 30 or 60 min later. As a result, the formation of F-actin bundles along cell-free edges and at cell–cell contact sites was inhibited, and a delay in the development of cell–cell adhesion was observed (lower panels in Fig. 4A,Ba). Quantitative analysis confirmed that attenuation of JRAB droplet formation induced by 1,6-HD significantly reduced the reformation of thick F-actin bundles along cell-free edges (Fig. 4Bb). We also examined whether attenuation of JRAB droplet formation affected re-establishment of cell–cell junctions. As an additional analysis, ZO-1 continuity was assessed after LatA treatment followed by 1,6-HD treatment. Consistent with the impaired F-actin bundle reformation, recovery of continuous ZO-1-positive junctions was also reduced by the treatment with 1,6-HD (Fig. S6).

Journal of Cell Science (2026) 139, jcs264804. doi:10.1242/jcs.264804

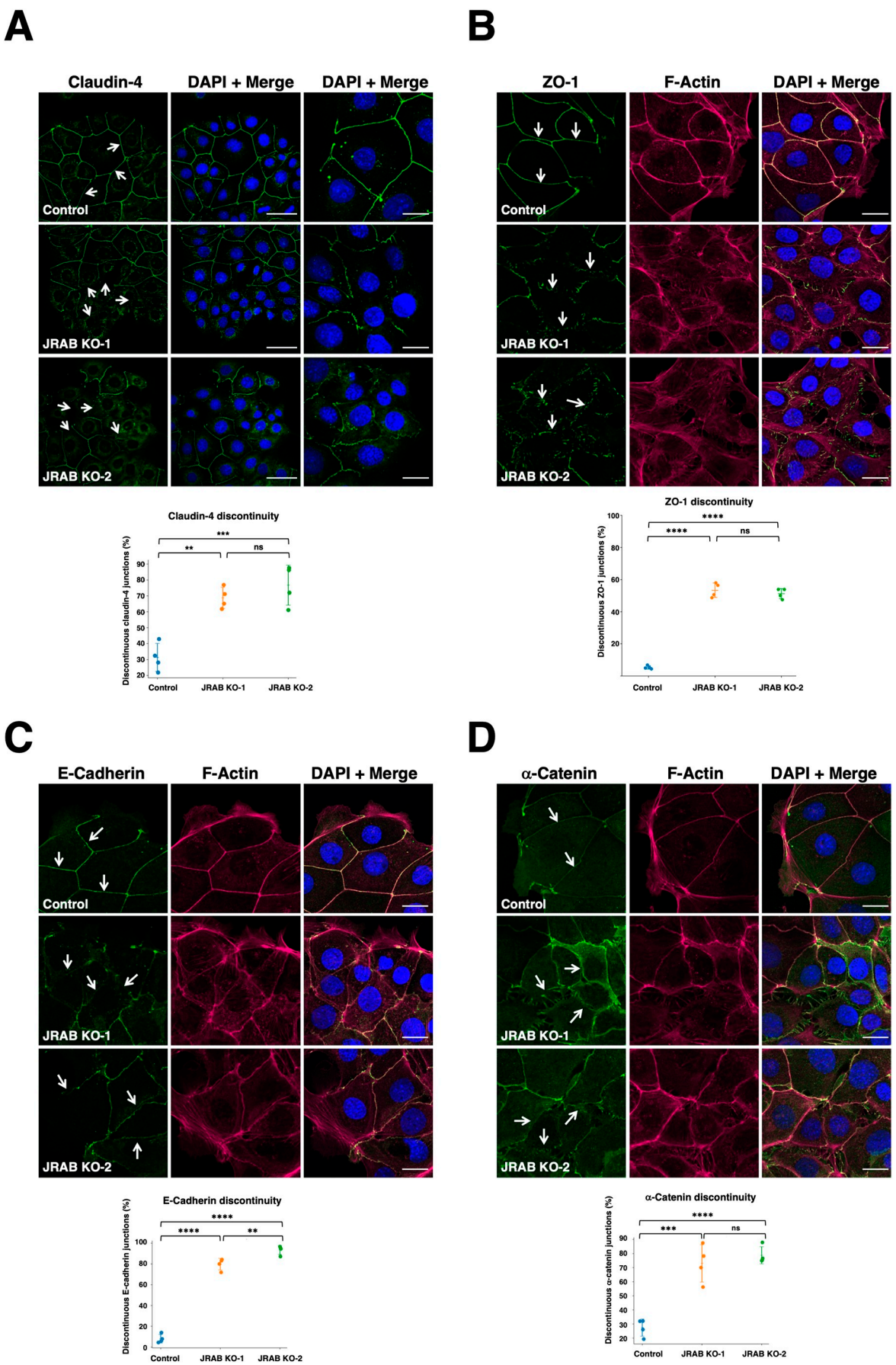


Fig. 2. See next page for legend.

Fig. 2. Effects of JRAB KO on cell–cell adhesion. Control cells and two independent JRAB KO cell lines (JRAB KO-1 and KO-2) were stained with anti-claudin-4 (A) and anti-ZO-1 (B) antibodies to visualize tight junctions (arrows), and with anti-E-cadherin (C) and anti-α-catenin (D) antibodies to visualize adherens junctions (arrows). F-actin was visualized with rhodamine–phalloidin (magenta), except in the cells stained with an antibody against claudin-4, which were fixed with methanol and therefore not stained with rhodamine–phalloidin. Nuclei were stained with DAPI (blue). Scale bars: 20 µm, except for the two left panels in A, for which the scale bars are 50 µm. Representative images from four independent experiments are shown. Adjacent graphs show quantification of discontinuous junctional structures identified by each target. Discontinuous junctions were expressed as a percentage of total junctional structures counted across multiple microscopic fields. Each dot represents one independent experiment (n=4). Bars indicate mean±s.d. **P<0.01; ***P<0.001; ****P<0.0001; ns, not significant (one-way ANOVA followed by Tukey's multiple comparisons test; control versus JRAB KO-1, P=0.00102; control versus JRAB KO-2, P<0.001; JRAB KO-1 versus JRAB KO-2, P=0.501 for claudin-4; control versus JRAB KO-1, P<0.0001; control versus JRAB KO-2, P<0.0001; JRAB KO-1 versus JRAB KO-2, P=0.6334 for ZO-1; control versus JRAB KO-1, P<0.0001; control versus JRAB KO-2, P<0.0001; JRAB KO-1 versus JRAB KO-2, P=0.0069 for E-cadherin; control versus JRAB KO-1, P=0.0002; control versus JRAB KO-2, P<0.0001; JRAB KO-1 vs JRAB KO-2, P=0.6556 for α-catenin).

These results suggest that JRAB droplets might contribute to the regulation of actin filaments at the free borders and cell–cell adhesion sites underlying the development of cell–cell adhesions.

JRAB droplets increase the formation of thick F-actin bundles, but JRAB in the fluid does not

We next investigated the function of JRAB droplets in the regulation of F-actin bundle morphology with *in vitro* experiments. GFP–JRAB formed liquid-like droplets in the presence of PEG (Fig. 5A), whereas no droplet formation was observed in the absence of PEG, consistent with our previous results (Sakane et al., 2021). We subsequently examined the effect of the JRAB droplets on the formation of F-actin bundles *in vitro*. GFP–JRAB droplets in the presence of PEG promoted F-actin assembly, resulting in the formation of thick F-actin bundles, whereas GFP–JRAB formed thin and faint F-actin bundles in the absence of PEG (Fig. 5Ba). These differences were confirmed by quantitative analysis of the thickness and fluorescence intensity of Alexa Fluor 647-labeled F-actin bundles (Fig. S7A). The association between the F-actin bundles and GFP–JRAB droplets was clearly observed using a Nikon's N-SIM super-resolution structured illumination microscopy system (Fig. S7B). In the absence of JRAB, F-actin bundles were scarcely observed even in the presence of PEG, which is known to promote bundle formation (Tang and Janmey, 1996), under the buffer conditions used in this study (Fig. S8). The molecular dynamics whereby GFP–JRAB moves from the droplet to F-actin bundle was also observed (Fig. 5Bb). In addition, analysis of the fluorescence recovery after photobleaching (FRAP) for GFP–JRAB on thick F-actin bundles revealed that GFP–JRAB was transferred from GFP–JRAB droplets to the thick F-actin bundle to which the GFP–JRAB droplets were closely associated (Movie 4, see also Fig. S14A,B, lower panels). Taken together, these findings suggest that JRAB liquid-like droplets increase the formation of thick F-actin bundles and that the JRAB transferred from droplets to F-actin bundles connects the small F-actin bundles, resulting in the stabilization of F-actin bundles.

JRAB forms liquid-like droplets together with Rab13

Previously, we reported that JRAB interacts with several molecules, such as Rab8A and Rab13, members of the small G protein Rab family (Terai et al., 2006; Yamamura et al., 2008), and actin cytoskeletal reorganization-related molecules such as actinin-1, actinin-4 and filaminA (Nakatsuji et al., 2008; Sakane et al., 2013). Consistent with previous reports, in our epithelial cell system, Venus–Rab13 prominently localized to cell–cell contact sites in addition to perinuclear regions, whereas GFP–Rab8A was mainly observed in perinuclear compartments, likely corresponding to recycling endosomes (Fig. S9). Rab13 is implicated in the regulation of tight junction formation and epithelial cell–cell adhesion (Marzesco et al., 2002; Köhler et al., 2004), whereas Rab8A is more broadly associated with membrane trafficking processes (Huber et al., 1993; Peränen, 2011). Therefore, we focused on Rab13 as the most relevant functional partner of JRAB in this study. JRAB localizes just beneath cell–cell contact sites together with Rab13, whereas along F-actin bundles at the cell-free border, JRAB localizes without Rab13 (Sakane et al., 2012). These observations led us to investigate the possibility that the JRAB–Rab13 complex might inhibit excessive F-actin bundling at cell–cell contact sites. We investigated the relationship between JRAB droplets and Rab13 in cells and *in vitro*. In epithelial cells co-expressing GFP–JRAB and a dominant-active (DA) mCherry–Rab13 mutant (Q67L) with impaired GTP hydrolysis (Marzesco et al., 2002), GFP–JRAB and mCherry–Rab13DA colocalized at cell–cell junctions in the absence of LatA (Fig. 6A, upper panels, arrows). After treatment with LatA, GFP–JRAB liquid-like droplets, including mCherry–Rab13DA, were observed in the cells (Fig. 6A, middle and lower panels, arrowheads). We also analyzed six cells from three independent experiments to examine the colocalization of GFP–JRAB and mCherry–Rab13DA within the droplets. The numbers of droplets containing GFP–JRAB and those containing mCherry–Rab13DA were very similar in all cells. Overall, 598 out of 604 GFP–JRAB droplets were colocalized with mCherry–Rab13DA, corresponding to 99.0% colocalization (Table S2). These results indicate that almost all GFP–JRAB-positive droplets contained mCherry–Rab13DA. Although fewer droplets were visually apparent after 1,6-HD treatment, the remaining GFP–JRAB-positive droplets retained strong colocalization with mCherry–Rab13DA (Fig. 6Ba,b). We also found that endogenous Rab13 was present in a subset of LatA-induced GFP–JRAB droplets, although the signal was weaker than that of overexpressed mCherry–Rab13DA (Fig. S10). These observations suggest that recruitment of Rab13 to JRAB droplets is not solely due to overexpression of mCherry–Rab13DA.

In vitro experiments using the recombinant proteins revealed that GFP–JRAB formed liquid-like droplets, including mCherry–Rab13DA (Fig. 6Ca). The recombinant protein mCherry alone was used as a negative control (Fig. S11). These results indicate that JRAB forms liquid-like droplets together with Rab13.

JRAB has different functions in F-actin bundling depending on the molecular composition of the droplet

Next, we examined the difference in the function of F-actin bundling among two kinds of JRAB droplets: JRAB alone and JRAB+Rab13. When Alexa Fluor 647-labeled F-actin was added to the GFP–JRAB+mCherry-Rab13DA droplets, fewer F-actin bundles formed (Fig. 6Cb), whereas the GFP–JRAB droplets formed thick F-actin bundles under the same experimental conditions (Fig. 6Cc). We quantified the area of fluorescently labeled F-actin bundles formed by GFP–JRAB droplets and GFP–JRAB+mCherry–Rab13DA droplets using three fields from three independent experiments. The analysis showed that GFP–JRAB droplets formed F-actin bundles with an ∼10-fold larger area than GFP–JRAB+mCherry-Rab13DA droplets (Fig. 6Cd). When scarce

Journal of Cell Science (2026) 139, jcs264804. doi:10.1242/jcs.264804

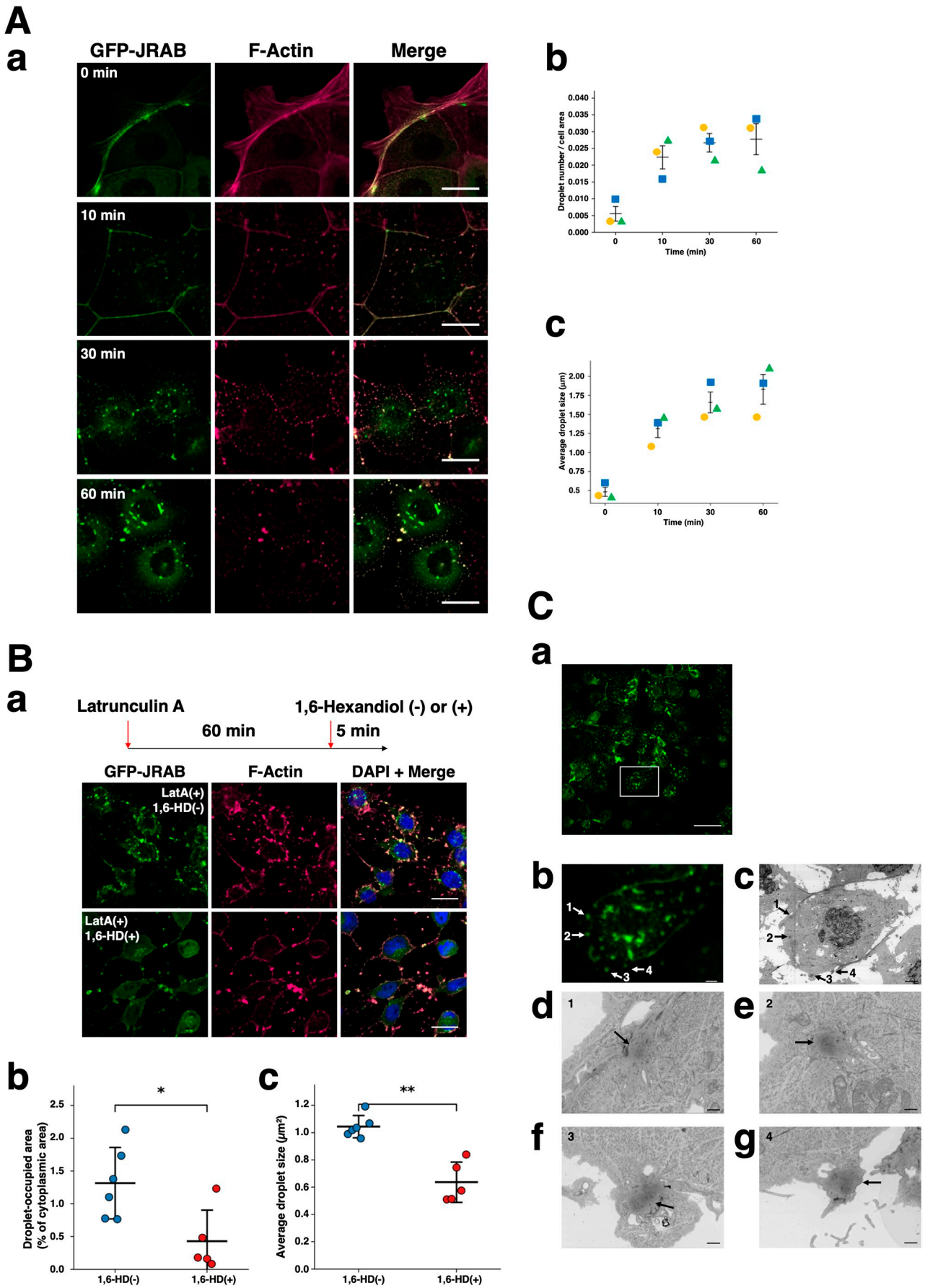


Fig. 3. See next page for legend.

Journal of Cell Science

Journal of Cell Science (2026) 139, jcs264804. doi:10.1242/jcs.264804

Fig. 3. Latrunculin A induces droplet-like structures containing JRAB in epithelial cells. (A) (a) MTD-1A cells expressing GFP–JRAB (green) were treated with latrunculin A (LatA) for the indicated times. The cells were fixed and stained with rhodamine–phalloidin (magenta). Scale bars: 20 µm. See also Movie 2. (b,c) Graphs show quantification of droplet density (droplet number normalized to cell area) and average droplet size, maximum length of a droplet (µm) over time. Circles, squares, and triangles represent independent experiments 1, 2 and 3, respectively. Each symbol represents one independent experiment (n=3). Horizontal bars and error bars indicate the mean±s.e.m. Data at each time point were obtained from independent experiments and do not represent repeated measurements of the same cells. (B) (a) MTD-1A cells expressing GFP–JRAB (green) were treated with LatA for 60 min, followed by incubation with 1,6-hexanediol (5% w/v) (1,6-HD) for 5 min. A schematic representation of the experimental protocol is presented. The cells were fixed and stained with rhodamine–phalloidin (magenta). Nuclei were stained with DAPI (blue). Scale bars: 20 µm. (b) The droplet-occupied area was significantly reduced by 1,6-HD treatment [1,6-HD(−), 1.31±0.54%; 1,6-HD(+), 0.43±0.47%; P=0.0182]. (c) The average droplet size was also significantly decreased [1,6-HD(−), 1.04±0.08 µm^2; 1,6-HD(+), 0.64±0.15 µm^2; P=0.0015]. (b,c) Each dot represents one independent experiment; bars indicate mean±s.d. *P<0.05; **P<0.01 [Welch's unpaired two-tailed t-test; blue, 1,6-HD(−); red, 1,6-HD(+)]. (C) Ultrastructural characterization of fluorescent droplet-like structures by CLEM. (a) GFP–JRAB-derived fluorescence image of cells treated with LatA for 60 min. (b) A higher-magnification fluorescence image of the boxed region in a, showing a cell containing representative fluorescent droplet-like structures (arrows and numbers). (c) Corresponding electron microscopy image of the same cell. Positions corresponding to the fluorescent structures in b are indicated by matching arrows and numbers. (d–g) Higher-magnification electron microscopy images of individual structures (1–4), showing amorphous, electron-dense regions. Within these regions, organelles such as ribosomes and mitochondria were rarely observed. The images in C were obtained from different regions of the same cell in a single CLEM experiment. Scale bars: 50 µm (a), 5 µm (b,c) and 500 nm (d–g).

F-actin bundles were observed, GFP–JRAB was found to be transferred onto the scarce F-actin bundles, whereas mCherry–Rab13DA was not (Fig. S12). These findings suggest that mCherry–Rab13DA inhibits the transfer of GFP–JRAB from droplet onto the F-actin bundle, thereby inhibiting the formation of thick F-actin bundles.

To examine whether the effect of Rab13 on JRAB-mediated F-actin bundling observed *in vitro* is reflected at the cellular level, we analyzed actin organization in MTD-1A cells coexpressing GFP–JRAB with either mCherry-Rab13DA or mCherry-Rab13 dominant-negative (DN) mutant (T22N), which has reduced affinity for GTP. Cells coexpressing GFP–JRAB and mCherry–Rab13DN frequently exhibited prominent thick F-actin bundles at the free edge, whereas these structures were markedly reduced in cells coexpressing GFP–JRAB and mCherry–Rab13DA. Quantitative analysis of the intensity of Alexa Fluor 647-labeled F-actin at the free edge confirmed a significant decrease in F-actin bundle formation in mCherry–Rab13DA-coexpressing cells compared with mCherry-Rab13DN-coexpressing cells (Fig. S13). These findings indicate that the functional state of Rab13 influences F-actin bundle organization at the cellular level, providing evidence consistent with our *in vitro* observations that Rab13 suppresses JRAB-mediated F-actin bundling.

Notably, although Rab13 mutants were analyzed in our previous study (Sakane et al., 2012), their effects on thick F-actin bundle formation at the free edge were not specifically examined. The present analysis extends these previous observations and suggests a role for Rab13 in regulating F-actin bundle organization associated with JRAB droplets.

Altogether, Rab13 may be a functional modulator of the increase in F-actin bundling via JRAB droplets. Specifically, JRAB exhibits different functions in F-actin bundling depending on the molecular composition of the droplet.

Differences in physical properties between the two kinds of droplets

Finally, we investigated the cause of the difference in the functions of JRAB droplets and JRAB+Rab13 droplets in the regulation of F-actin bundles. GFP–JRAB droplets were smooth and spherical, whereas GFP–JRAB+mCherry–Rab13DA droplets were irregular in shape (Fig. 7A). To examine whether this morphological difference reflects distinct mechanical properties, we measured droplet stiffness using high-speed atomic force microscopy (HS-AFM)-based high-speed in-line force mapping (HS-iFM) (Ganser et al., 2025). The elastic modulus was measured for 20 GFP–JRAB droplets and 22 GFP–JRAB+mCherry–Rab13DA droplets. The stiffness of both droplets is shown in Fig. 7B. The stiffness of the GFP–JRAB droplets was 153±36 kPa (mean±s.d.), whereas the stiffness of the GFP–JRAB+mCherry–Rab13DA droplets was 228±81 kPa. This difference in stiffness was significant according to a Welch test (Welch, 1947), with a significance level of 5.0×10^{-4}. These quantitative measurements indicate that the incorporation of Rab13 significantly increases droplet stiffness by ∼50%. This finding indicates that the increased stiffness of GFP–JRAB+mCherry–Rab13DA droplets could be a consequence of increased internal bonds in the presence of Rab13, making the droplets more stable and less likely to interact with F-actin for bundle formation.

Polymer network theory predicts that an increased density of interacting sites both increases the elastic modulus and decreases the mobility of the constituent molecules (Jawerth et al., 2020; Rubinstein and Semenov, 1998; Wang et al., 2018). We therefore examined whether the increased stiffness of GFP–JRAB+mCherry–Rab13DA droplets is accompanied by a reduced mobility of GFP–JRAB, using FRAP (Fig. 7C; Fig. S14). The mobile fraction of GFP–JRAB was ∼30% lower in GFP–JRAB+mCherry–Rab13DA droplets than in GFP–JRAB droplets, although this difference did not reach statistical significance with the sample sizes examined (P=0.060; n=12 and 20). GFP–JRAB on F-actin bundles showed the highest mobile fraction, which was significantly higher than that in GFP–JRAB+mCherry–Rab13DA droplets (P=0.014) but not significantly different from that in GFP–JRAB droplets (P=0.13).

Thus, two independent measurements of the same droplets – the elastic modulus, which was significantly increased, and the mobile fraction, which was reduced by ∼30% – both changed in the direction predicted by polymer network theory. These results indicate that the incorporation of Rab13 restricts the exchange of JRAB within the droplet, thereby limiting its availability for transfer onto F-actin bundles.

DISCUSSION

JRAB is an effector protein for Rab13 (Terai et al., 2006; Yamamura et al., 2008). Rab13 is localised mainly on the plasma membrane. The JRAB–Rab13 complex contributes to cell adhesion through the transport of cell adhesion molecules to the plasma membrane (Sakane and Sasaki, 2015; Sakane et al., 2012; Terai et al., 2006; Yamamura et al., 2008). Additionally, JRAB plays multiple roles in the spatiotemporal rearrangement of the actin cytoskeleton during collective cell migration (Sakane et al., 2016). However, how JRAB achieves such spatial and qualitative control of actin filaments has remained unclear. Therefore, in this study, we first generated JRAB KO cells and examined in detail the effects of JRAB deficiency on the spatial organization and properties of actin

Journal of Cell Science (2026) 139, jcs264804. doi:10.1242/jcs.264804

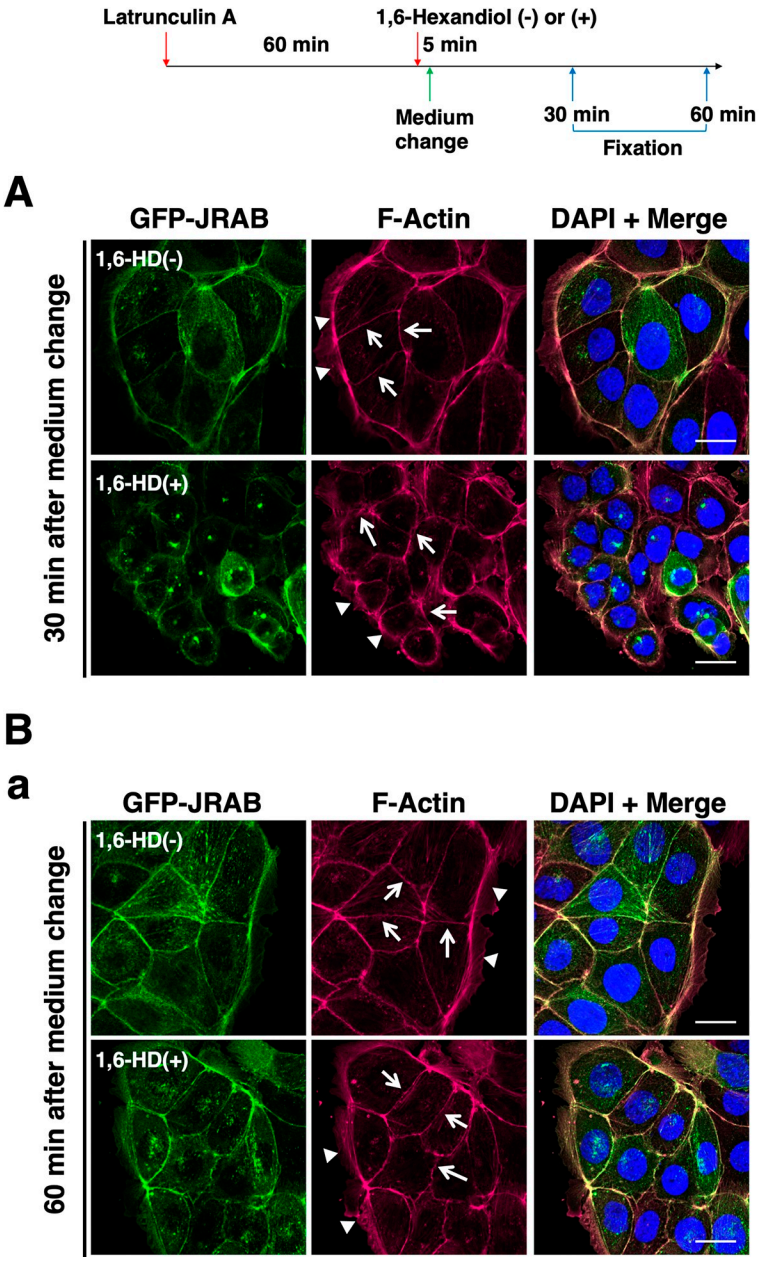


Fig. 4. JRAB droplets regulate actin filaments at the free border and cell–cell adhesion sites of epithelial cells. A schematic representation of the experimental protocol is presented. (A,Ba) Upper panels, MTD-1A cells expressing GFP–JRAB (green) were treated with LatA for 60 min. After LatA was removed from the cells, the GFP signal (green) of the droplet-like structure disappeared, and reconstruction of F-actin bundles along cell-free borders (arrowheads) and at cell–cell contacts (arrows) was observed at the indicated times. Lower panels, MTD-1A cells expressing GFP–JRAB (green) were treated with LatA for 60 min, followed by incubation with 1,6-HD for 5 min. After 1,6-HD was removed from the cells, the reconstruction of the F-actin bundles along cell-free borders (arrowheads) and at cell–cell contacts (arrows) was still disrupted 60 min after the medium change. F-actin and nuclei were visualized with rhodamine–phalloidin (magenta) and DAPI (blue), respectively. Scale bars: 20 µm. Representative images from four independent experiments are shown in A and Ba. (Bb) The percentage of free edges exhibiting thick F-actin bundles was quantified at the 60 min time point shown in Ba. Each dot represents one independent experiment (n=4). Bars indicate mean±s.d. Treatment with 1,6-HD markedly reduced the proportion of free edges containing thick F-actin bundles [1,6-HD(−): 58.8±5.9%, 1,6-HD(+): 24.1±2.4%; P<0.001]. ***P<0.001 (Welch's two-tailed unpaired t-test).

filaments. JRAB deficiency perturbed the formation of thick F-actin bundles along the free border of the cells, followed by impaired maturation of FAs. In addition, F-actin bundles just beneath cell–cell adhesions were disrupted, leading to the collapse of intercellular adhesion structures (e.g. TJs and AJs). These results emphasize the important role of JRAB in the actin dynamics involved in the development of cell–cell adhesions.

An important question is how JRAB regulates actin organization during this process. JRAB has an intrinsically disordered region (IDR) between its N-terminal LIM domain and C-terminal coiled-coil domain, suggesting its potential to form biomolecular condensates. Indeed, our previous work revealed that JRAB forms phase-separated droplets together with Rab8A (Sakane et al., 2021). Although Rab8A and Rab13 are closely related Rab proteins that share JRAB as a common effector protein, they differ in their subcellular localization and cellular functions. Rab8A is mainly observed in perinuclear recycling endosomes and broadly associated with membrane trafficking processes (Huber et al., 1993; Peränen, 2011). We have previously shown that JRAB+Rab8A droplets function to deform the membrane of recycling endosomes and induce the formation of tubular structures (Sakane et al., 2021). In this study, we found that JRAB liquid-like droplets function not only in organelle membrane deformation but also in the regulation of F-actin bundling. We speculate that JRAB forms droplets via LLPS because JRAB droplets, where JRAB is locally concentrated, interact with F-actin more efficiently than uniformly diffusing JRAB. This localized interaction could act as a platform for the gathering and bundling of F-actin, ultimately facilitating the formation of thick F-actin bundles. We also observed the continuous localization of JRAB along the F-actin bundles formed by JRAB droplets *in vitro* experiments. Furthermore, we obtained STED super-resolution images

Journal of Cell Science (2026) 139, jcs264804. doi:10.1242/jcs.264804

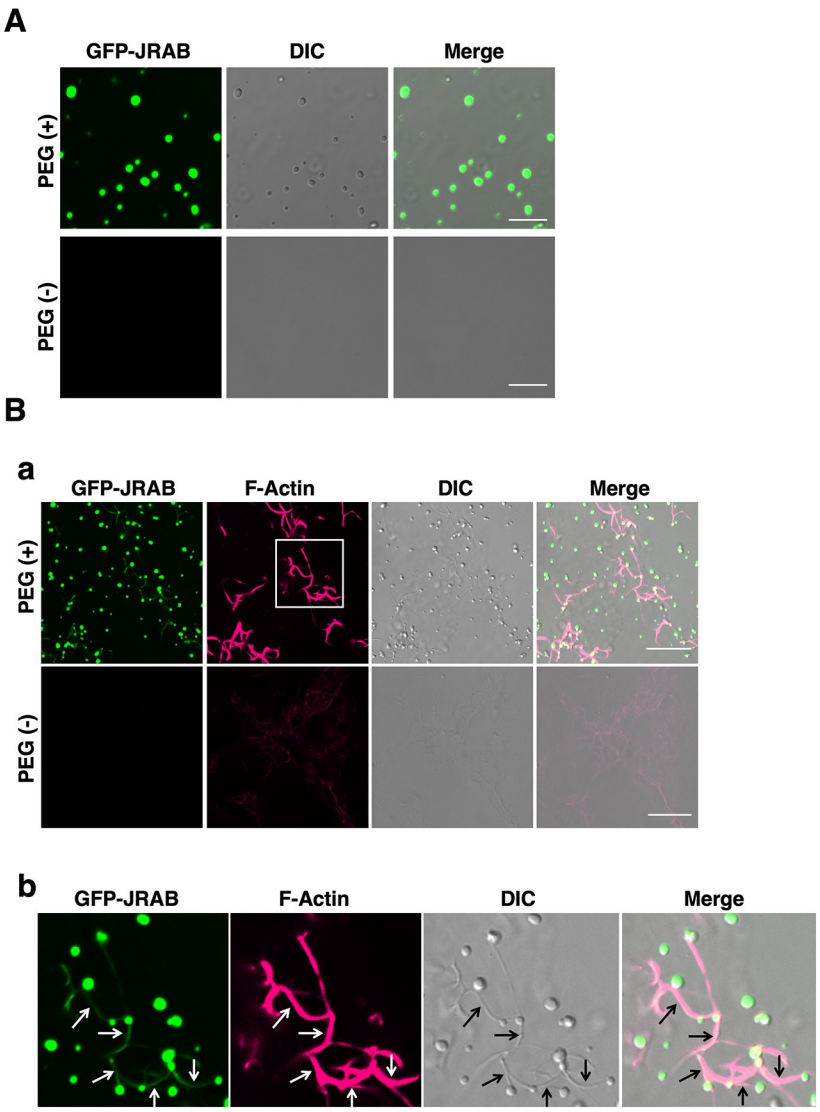


Fig. 5. JRAB droplets form thick and straight F-actin bundles, but JRAB in a fluid state does not. (A) Upper panels, His–GFP–JRAB (green) exhibited liquid-like droplet formation upon the addition of a crowding agent (4.3% PEG). Lower panels, no droplet formation was observed in the absence of PEG. Scale bars: 10 µm. (B) (a) Upper panels, Alexa Fluor 647-labeled F-actin (magenta) was added to GFP–JRAB (green) in the presence of 4.3% PEG. Lower panels, Alexa Fluor 647-labeled F-actin (magenta) was added to GFP–JRAB (green) in the absence of 4.3% PEG. Scale bars: 20 µm. (b) Higher-magnification views of the region enclosed by the square in the upper panel in a. Arrows indicate that GFP–JRAB moves from the droplet to the F-actin bundle. Representative images from three independent experiments are shown in A and B.

suggesting that the JRAB droplets connected actin fibers in this study. These observations lead us to speculate that JRAB, which binds sporadically to actin fibers as a droplet, might be transferred onto the fibers, coat the actin fiber surface and function as an interfiber bridge.

Rab13 was recruited into JRAB droplets, where it was shown to negatively regulate the F-actin bundling activity of JRAB droplets. When F-actin was added to GFP–JRAB+mCherry–Rab13DA droplets *in vitro*, GFP–JRAB – but not mCherry-Rab13DA – was detected on the barely formed F-actin bundle. Taken together, these results raise the possibility that the following cellular events occur: (1) JRAB forms liquid-like droplets and locally increases its concentration to promote efficient F-actin bundle formation; (2) JRAB then transfers from the droplet to the surface of F-actin bundles, which stabilizes them, with Rab13 predicted to regulate this entire process (Fig. 8). We propose a difference in the physical properties (stiffness) between JRAB droplets and JRAB+Rab13 droplets as one of the factors underlying the suppression of F-actin bundle formation by JRAB+Rab13 droplets. HS-AFM-based HS-iFM analyses revealed that when mCherry–Rab13DA was incorporated into GFP–JRAB droplets, both their morphology and mechanical properties, such as stiffness, were altered. The stiffness values of the GFP–JRAB droplets and the GFP–JRAB+mCherry–Rab13DA droplets were generally greater than those reported for the gel phases of plant protein LLPS droplets, which range from 5 kPa to 100 kPa (Hutin et al., 2023). However, because LLPS droplets are highly viscoelastic, the elastic modulus depends on the loading rate. The loading rate reported by Hutin et al. (2023) was 10 µm/s, whereas the elastic modulus values of GFP–JRAB and GFP–JRAB+mCherry–Rab13DA droplets were recorded as 600 µm/s. This is consistent with viscoelasticity, in which a higher loading rate leads to a higher modulus, as described by Rubinstein and Semenov for polymer gelation (Rubinstein and Semenov, 1998), but also describes the properties of LLPS (Jawerth et al., 2020; Wang et al., 2018). This theory also links the density of so-called ‘stickers’ – interacting sites – with the elastic modulus, where the elastic modulus increases with increasing sticker density. These findings indicate that the increased stiffness of JRAB+Rab13 droplets could be a consequence of increased internal bonds in the presence of Rab13, making the droplets more stable and less likely to interact with actin filaments for bundle formation. Additionally, the increased stiffness of the droplets might not allow JRAB to move from the droplet to F-actin. Furthermore, we speculate that this

Journal of Cell Science (2026) 139, jcs264804. doi:10.1242/jcs.264804

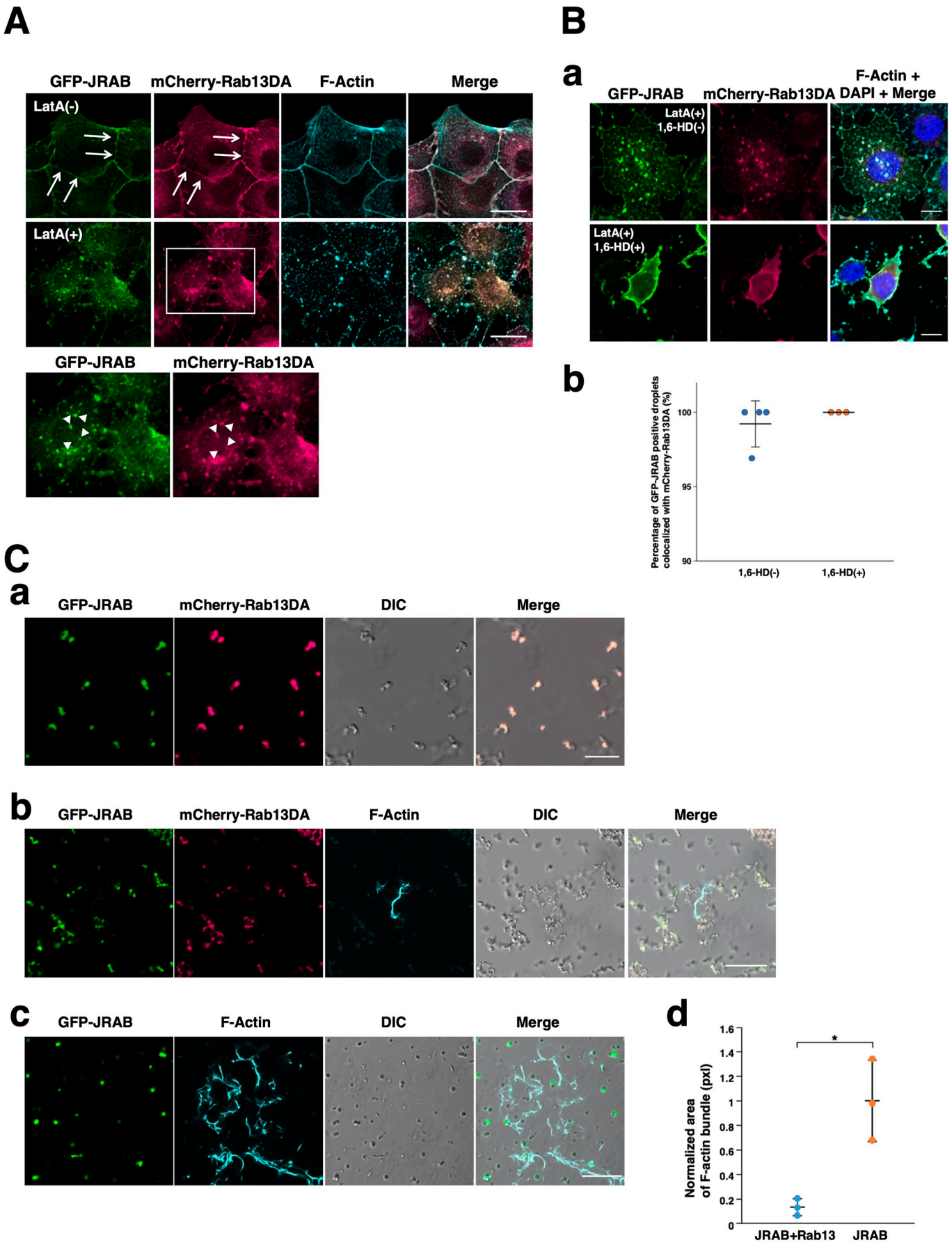


Fig. 6. See next page for legend.

Journal of Cell Science

Journal of Cell Science (2026) 139, jcs264804. doi:10.1242/jcs.264804

Fig. 6. JRAB forms liquid-like droplets together with Rab13. (A) MTD-1A cells expressing GFP–JRAB (green) and mCherry–Rab13DA (magenta) were treated with LatA. The cells were fixed and stained with Alexa Fluor 647-labeled phalloidin (light blue). Upper panels, before the addition of LatA. Arrows indicate the cell–cell adhesion sites. Middle panels. 30 min after the addition of LatA. Scale bars: 20 µm. Lower panels, higher-magnification views of the regions enclosed by the rectangle in the middle panel. Arrowheads indicate liquid-like droplets containing both GFP–JRAB and mCherry–Rab13DA. Colocalization of GFP–JRAB-positive droplets with mCherry–Rab13DA is quantified in Table S2. (B) (a) MTD-1A cells expressing GFP–JRAB (green) and mCherry–Rab13DA (magenta) were treated with LatA for 60 min, followed by incubation with 1,6-HD for 5 min. F-actin and nuclei were visualized with Alexa Fluor 647-labeled phalloidin (light blue) and DAPI (blue), respectively. Scale bars: 10 µm. (b) The percentage of GFP–JRAB-positive droplets colocalized with mCherry–Rab13DA was quantified before and after 1,6-HD treatment. Each dot represents one independent experiment [n=4 for 1,6-HD(−) and n=3 for 1,6-HD(+)]. Bars indicate mean±s.d. (C) (a) His–GFP–JRAB (green) and His–mCherry–Rab13DA (magenta) exhibited liquid-like droplet formation in the presence of 4.3% PEG. Scale bar, 10 µm. (b) Alexa Fluor 647-labeled F-actin (light blue) was added to liquid-like droplets containing GFP–JRAB (green) and mCherry–Rab13DA (magenta) in the presence of 4.3% PEG. Scale bar: 20 µm. (c) Alexa Fluor 647-labeled F-actin (light blue) was added to liquid-like droplets containing GFP–JRAB (green) alone in the presence of 4.3% PEG. The experiments were performed under the same experimental conditions as in b with the sole exception that mCherry–Rab13DA was omitted. Scale bar: 20 µm. (d) Quantification of the area of the fluorescent F-actin bundles. Data are presented as mean±s.d. (n=3). *P<0.05 (Welch's unpaired two-tailed t-test; P=0.0407. Representative images from three or four independent experiments are shown in A, Ba and C.

increased stiffness of the droplets physically constrains the mobilization of JRAB from the droplet to the F-actin bundle, thereby hindering bundle stabilization. Using FRAP, we confirmed that GFP–JRAB has a higher mobile fraction compared to GFP–JRAB+mCherry–Rab13DA, which is consistent with the theory of interacting sites, or stickers. GFP–JRAB+mCherry–Rab13DA droplets show a reduction in the mobile fraction, which would be a consequence of an increased density of stickers, hindering the free movement of GFP–JRAB. GFP–JRAB on actin filaments, however, showed mobility comparable to that of GFP–JRAB droplets – as seen in FRAP measurements – meaning that it can move along the fibril bundles.

Unlike canonical MICAL proteins, which directly promote F-actin disassembly through redox-dependent mechanisms (Giridharan and Caplan, 2014; Giridharan et al., 2012), JRAB lacks monooxygenase activity and has been proposed to function as a scaffold protein (Miyake et al., 2019; Nakatsuji et al., 2008; Sakane et al., 2012, 2013). Our findings provide a potential mechanism for this distinct mode of actin regulation by showing that JRAB forms condensates that promote the organization of F-actin into distinct structures. Thus, JRAB appears to regulate the actin cytoskeleton through a condensate-based mechanism that is distinct from the enzymatic activity of canonical MICAL proteins. These findings broaden the functional framework of the MICAL family, suggesting that its members can regulate the actin cytoskeleton not only through enzymatic modification of actin but also through scaffold- and condensate-based mechanisms.

We previously reported that JRAB associates with actinin-1 and -4 upon its binding to Rab13 (Nakatsuji et al., 2008; Sakane et al., 2013). α-Actinin (ACTN) proteins are well-characterized actin-crosslinking proteins that crosslinks actin filaments at defined, regular intervals along the filaments. These proteins form actin filament bundles through their N-terminal actin-binding domains. Their antiparallel dimerization enables them to crosslink adjacent actin filaments. By contrast, because JRAB possesses actin-binding domains at its N-terminus and central region, it might not crosslink individual actin filaments in an ACTN-like manner. Instead, by acting as a droplet, JRAB could roughly bundle groups of actin filaments together in a glue-like fashion. JRAB might subsequently relocate from within JRAB droplets to the surface of actin filaments or to the spaces between actin filaments, thereby reinforcing the F-actin bundles as described above. Although actinin-1 and -4 are thought to function cooperatively with Rab13, further analyses are needed to clarify their role in the function of JRAB droplets. Alternatively, actin-crosslinking proteins, including actinin-1 and -4, might also be capable of forming droplets. In this study, JRAB droplets served as a representative example for understanding the relationship between droplets and the regulatory mechanism of F-actin bundles, and extending this analysis to other actin-crosslinking proteins will be important for future work.

The results of the present study revealed that JRAB droplets play a crucial role in mediating the crosstalk between the intracellular transport of adhesion molecules and actin cytoskeletal reorganization during the development of cell–cell adhesions. It has been reported that, at the early stages of autophagosome formation, droplets are formed by Atg-related molecules, into which Atg vesicles are incorporated, thereby generating the origin of the isolation membrane (Fujioka et al., 2020; Sawa-Makarska et al., 2020). Therefore, it is important to clarify the relationship between JRAB droplets and the intracellular transport of adhesion molecules (e.g. transporting vesicles) in future studies.

In addition, it has been reported that the TJ component ZO-1 undergoes phase separation just beneath the plasma membrane to form liquid-like droplets that regulate actin filament polymerization and the lateral diffusion of claudins, thereby contributing to junction assembly (Beutel et al., 2019; Pombo-García et al., 2024; Schwayer et al., 2019; Sun et al., 2025). However, the findings in this study introduce a new concept in which the function of a droplet is modulated by other molecules within the droplet itself. In future studies, we aim to investigate the relationship between JRAB droplets and ZO-1 droplets.

The role of JRAB droplets *in vivo* remains an important issue that has yet to be elucidated. It has been reported that Rab13 knockout mice largely develop normally. In addition, we have already generated and analyzed JRAB KO mice (A. Sakane, unpublished data). In contrast to the phenotypes anticipated from the analyses of JRAB KO cells, this mutation was not embryonically lethal and caused no apparent abnormalities in organ or tissue development. These observations suggest the existence of redundant systems and compensatory gene expression that might mitigate the effects of gene knockout. Analyses such as RNA-seq of control and KO mice, as well as control and KO cells, could help to elucidate the underlying mechanisms and provide insight into the observed phenotypes. Despite these findings in the highly complex and tightly regulated *in vivo* environment, our *in vitro* analyses enabled the identification of a previously unrecognized regulatory mechanism of actin dynamics mediated by JRAB droplets. Accordingly, further investigations are needed to determine when and where JRAB droplets are present *in vivo* and to define their functional significance.

Taken together, our findings reveal a previously unrecognized principle whereby the functions of liquid-like droplets are governed by the diversity of their molecular components. This discovery represents a conceptual advance that is expected to have broad implications across diverse research fields, extending beyond the field of LLPS.

Journal of Cell Science (2026) 139, jcs264804. doi:10.1242/jcs.264804

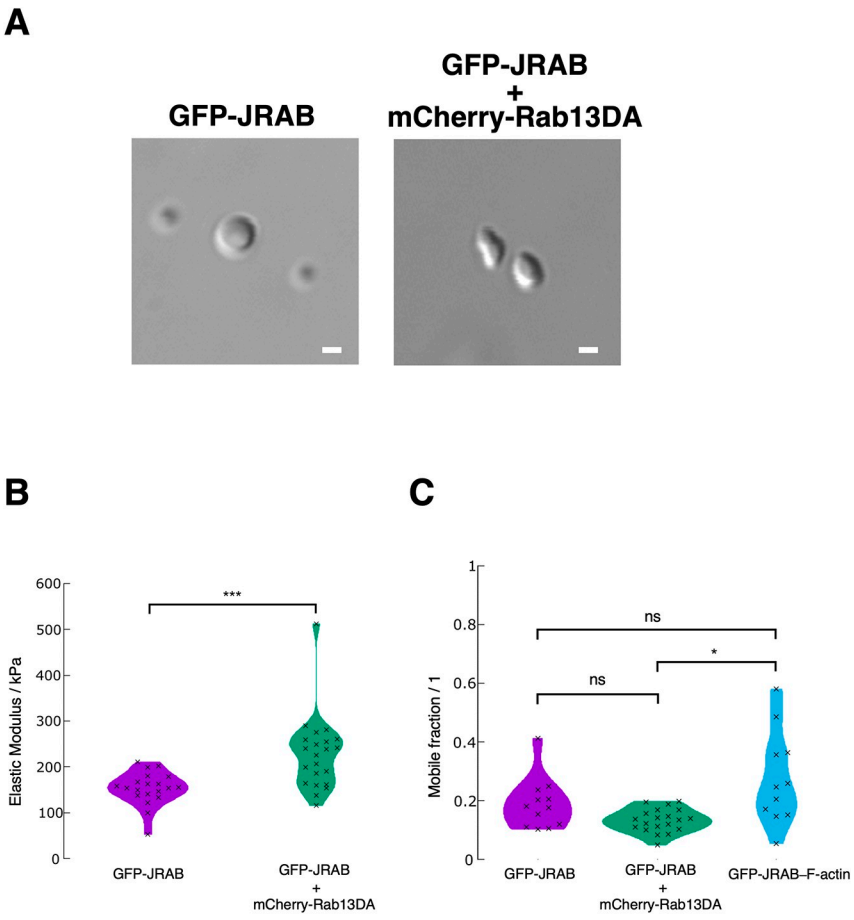


Fig. 7. Differences in physical properties between the two kinds of droplets. (A) Left panel, GFP–JRAB droplets. Right panel, GFP–JRAB droplets containing mCherry–Rab13DA. Scale bars: 1 µm. (B) Violin plot of the elastic modulus of GFP–JRAB (n=20) and GFP–JRAB+mCherry–Rab13DA (n=22) droplets. The stiffness of the GFP–JRAB droplets was 153±36 kPa (mean±s.d.), whereas the stiffness of the GFP–JRAB+mCherry–Rab13DA droplets was 228±81 kPa. ***P<0.001 (unpaired two-tailed Welch's t-test; P=0.0005). (C) Violin plot of the mobile fraction determined by FRAP for GFP–JRAB droplets (n=12), GFP–JRAB+mCherry–Rab13DA droplets (n=20) and GFP–JRAB on F-actin bundles (n=11). *P<0.05; ns, not significant (using unpaired two-tailed Welch's t-tests for three pre-planned comparisons, without correction for multiple comparisons: GFP–JRAB versus GFP–JRAB+mCherry–Rab13DA, P=0.060; GFP–JRAB+mCherry–Rab13DA versus GFP–JRAB–F-actin, P=0.014; GFP–JRAB versus GFP–JRAB–F-actin, P=0.13).

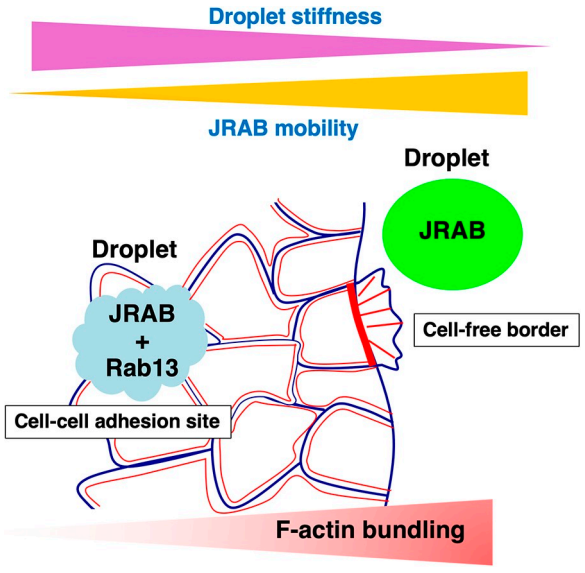


Fig. 8. Working model of actin dynamics controlled by JRAB droplets. JRAB droplets induce the formation of thick and straight F-actin bundles at the free edge of the cell population, whereas JRAB+Rab13 droplets inhibit excessive F-actin bundling at the cell–cell adhesion sites. Changes in the molecular composition of JRAB droplets alter their stiffness, which is inversely related to the mobility of JRAB within the droplets. Thus, JRAB droplets organize spatiotemporal F-actin dynamics by changing its molecular composition and biophysical properties. The red lines represent actin filaments.

MATERIALS AND METHODS

Plasmid construction

To produce retroviruses-expressing GFP-, Venus- or mCherry-tagged proteins, we generated pMX-EGFP, pMX-Venus, and pMX-mCherry from the pMX vector as described previously (Sakane et al., 2012). cDNAs encoding mouse JRAB, Rab13, Rab8A, a Rab13 dominant-active (DA) mutant (Q67L), a Rab13 dominant-negative (DN) mutant (T22N), or paxillin were subcloned and inserted into pMX-EGFP, pMX-Venus, or pMX-mCherry. To produce hexahistidine (His6)-GFP-tagged and His6-mCherry-tagged recombinant proteins, we generated pcDNAHisMax-EGFP and pcDNAHisMax-mCherry from the pcDNAHisMax vector as described previously (Sakane et al., 2021). cDNAs encoding JRAB and Rab13DA were subcloned and inserted into pcDNAHisMax-EGFP and pcDNAHisMax-mCherry, respectively. All plasmids constructed in this study were sequenced using an ABI Prism 3100 genetic analyzer (Applied Biosystems).

Construction of lentiviral transfer plasmid DNA

pCS-CMV-Venus and pX330-U6-ChimericBB-CBh-hSpCas9 (Cong et al., 2013) were obtained from the RIKEN BioResource Center (Tsukuba, Japan) and Addgene (Addgene #42230), respectively. Their components were utilized to construct a single lentiviral transfer plasmid DNA consisting of Cas9 and single guide RNA expression cassettes. A pair of synthetic nucleotides corresponding to the T2A peptide (EGRGSLLTCGDVEENPGP) was ligated upstream of the Venus cDNA, after which the T2A–Venus fragment was inserted downstream of the hSpCas9 cDNA in which the stop codon was absent, resulting in the plasmid designated pU6-Chimeric-CBh-Cas9-T2A-Venus. The fragment of the CRISPR components in the plasmid was introduced upstream of the woodchuck hepatitis virus posttranscriptional regulatory element in pCS-CMV-MCS (RIKEN BioResource Center) after removal of the CMV promoter, resulting in the plasmid designated pCS-U6-Chimeric-CBh-Cas9-T2A-Venus. In the

lentiviral CRISPR/Cas9 transfer plasmid, two *Bsm*BI recognition sequences, 5′-GGAGACGTTCGAACGTCTCG-3′, were inserted just downstream of the U6 promoter in place of the BbsI recognition sequence of the original plasmid (Cong et al., 2013). Synthetic oligonucleotides for sense and antisense sequences corresponding to guide RNA against mouse *JRAB* (NM174850) (5′-CACCGGCAGCAGTGCGAGGGCTAC-3′, 5′-AAACGTAGCCCTCGCACTGCTGCC-3′) were annealed, phosphorylated, and inserted between two *Bsm*BI sites in the plasmid pCS-U6-Chimeric-CBh-Cas9-T2A-Venus.

Antibodies and probes

Information on the antibodies and probes used in this study is provided in Table S3.

Chemicals and reagents

Latrunculin A (LatA) was obtained from Cayman Chemical. 1,6-Hexanediol was purchased from Sigma-Aldrich. The DAPI used for nuclear staining was obtained from KPL (SeraCare).

Cell culture

MTD-1A cells were a kind gift from Dr Shoichiro Tsukita (Kyoto University, Kyoto, Japan). MTD-1A cells were cultured in Dulbecco's modified Eagle's medium (DMEM; nacalai tesque #08458-16) supplemented with 10% fetal bovine serum (FBS; Biosera FB-1285/500), 100 U/ml penicillin, and 100 µg/ml streptomycin (nacalai tesque #26253-84). HEK293 cells were obtained from Dr Yoshimi Takai (Kobe University, Kobe, Japan). HEK293 cells were cultured in DMEM supplemented with 5% FBS, 1 mM sodium pyruvate, 100 U/ml penicillin and 100 µg/ml streptomycin. Both MTD-1A and HEK293 cells were maintained at 37°C in a water-saturated atmosphere of 95% air and 5% CO_2.

Recombinant retrovirus infection

The pMX-EGFP vector containing JRAB or paxillin and the pMX-mCherry vector containing Rab13DA or Rab13DN were separately transfected into PLAT-E cells as described previously (Sakane et al., 2012). After a 48-h transfection, each culture supernatant was collected and filtered through a 0.45-µm filter prior to infection. MTD-1A cells were infected either with each recombinant retrovirus separately or with a combination of recombinant retroviruses. After a 48-h culture period, the cells were subjected to further experiments.

Preparation of JRAB KO MTD-1A cells via an integration-defective lentiviral vector

To generate JRAB knockout (KO) MTD-1A cells, an integration-defective lentiviral vector (IDLV) carrying the CRISPR components was prepared as follows. Vectors pseudotyped with vesicular stomatitis virus glycoprotein G (VSV-G) were generated by standard DNA transfection (Philippe et al., 2006; Wanisch and Yáñez-Muñoz, 2009). Packaging plasmid DNAs, pCMV-VSV-G-RSV-Rev, pCAG-HIVgp, and pCAG-HIVgp IN-D64V, were obtained from RIKEN BioResource Center. To prepare the IDLV, the pCAG-HIVgp IN-D64V packaging plasmid was used instead of pCAG-HIVgp (Philippe et al., 2006; Wanisch and Yáñez-Muñoz, 2009). HEK293T cells (RIKEN Cell Bank in RIKEN Bioresource Center) were transfected with the transfer, envelope, and packaging plasmids using Lipofectamine LTX (Life Technologies). The IDLV particles were collected by ultracentrifugation at 50,000 rpm (100,000 ***g***) for 1 h using a centrifuge (Beckman Coulter, Optima MAX-XP) equipped with a rotor (MLS-50) and resuspended in DMEM.

MTD-1A cells (2×10^4 cells/well) were cultured on 24-well culture plates and transduced with 50 µl of the IDLV (MOI=50). At 2 days after transduction, individual cells were cloned onto 96-well culture plates by limiting dilution and maintained in culture. Each of the established cell lines was characterized by western blotting.

Cell sorting

MTD-1A cells expressing GFP–JRAB, or GFP–paxillin, Venus–Rab13 or GFP–Rab8A, coexpressing GFP–JRAB with either mCherry–Rab13DA or mCherry–Rab13DN, as well as JRAB KO MTD-1A cells expressing GFP–JRAB or GFP–paxillin were sorted based on fluorescence intensity using a BD FACSAriaII (BD Biosciences), CytoFlex SRT (Beckman Coulter), or a JSAN desktop cell sorter (Bay Bioscience, Kobe, Japan). Cells exhibiting fluorescence within a selected intensity range were collected to obtain cell populations with relatively uniform expression levels.

Western blotting

The cell lysates were separated by SDS-PAGE, transferred to Immobilon-P membranes (Merck), and blocked for 1 h in Tris-buffered saline supplemented with 5% non-fat dry milk. After the membranes were incubated with specific primary antibodies for 1 h and then with HRP-coupled secondary antibodies for 1 h (Table S3), the immunoreactive proteins were visualized using Western blotting Substrate Plus (Pierce). Full uncropped images of all western blots are shown in Fig. S15.

Latrunculin A treatment and washout assay

Cells were treated with latrunculin A (LatA) by replacing the culture medium with fresh medium containing LatA at a final concentration of 1 µM and incubation for 1 h. For time-course analysis, cells were incubated with LatA and fixed at the indicated time points. For washout experiments, after 1 h incubation with LatA, cells were washed twice with PBS and further incubated in LatA-free medium, then fixed at the indicated time points. In parallel, live-cell imaging was performed before and after LatA washout.

Immunocytochemical staining and confocal laser scanning microscopy

MTD-1A cells were seeded at a density of 2×10^5 cells on coverslips in individual 35-mm dishes or in 35-mm glass-bottom dishes. The following day, the cells were incubated with the indicated reagents for the indicated times. Afterward, the cells were fixed with 1% or 2% paraformaldehyde (PFA) in PBS at room temperature for 20 min, except for staining with the anti-claudin-4 antibody, for which cells were fixed with methanol at −20°C for 5 min. After being washed with PBS, the cells were incubated in 5% donkey serum (Jackson ImmunoReasearch, #017-000-121) and 0.1% Triton X-100 in PBS for 30 min. Next, the cells were incubated with primary antibodies for 1 h (Table S3), followed by incubation with fluorescent dye-conjugated secondary antibodies (Jackson ImmunoResearch, Invitrogen) for 1 h. F-actin was labeled with rhodamine–phalloidin or Alexa Fluor 647–phalloidin (Invitrogen). Coverslips were mounted on glass slides, and the samples were observed using an A1 or AX confocal laser scanning microscope (Nikon) equipped with an oil objective lens (PlanApo VC 60×, NA=1.4) and excitation lasers (488, 561 and 640 nm, COHERENT). The images shown are representative of at least three independent experiments.

Junctions showing one or more interruptions in continuous claudin-4 (or ZO-1, E-cadherin or α-catenin) staining along the cell–cell boundary were scored as discontinuous junctions.

Quantification of focal adhesion length

FAs were identified by vinculin immunostaining within a 5-µm-wide peripheral region of each cell. After Gaussian filtering, FAs were segmented using Otsu automatic thresholding in Fiji software. Objects with an area <0.3 μm^2 or a Feret diameter <0.5 µm were excluded. The Feret diameter of each remaining FA was measured and used for object-level analysis. The cumulative distribution of focal adhesion length was generated from all detected focal adhesions in each experimental group. For experiment-level comparisons, the mean focal adhesion length and the percentage of long FAs (Feret diameter >2 µm) were calculated for each independent experiment.

Live-cell imaging of focal adhesions

Control and JRAB KO-1 cells stably expressing GFP–paxillin were observed by total internal reflection fluorescence (TIRF) microscopy using a Nikon Ti-E equipped with an oil-immersion objective lens (PlanApo TIRF 60×, NA=1.45) and a Zyla sCMOS camera (Andor Technology). Images were acquired at 1-min intervals for 60 min. GFP–paxillin-positive FAs were tracked over time, and GFP–paxillin fluorescence intensity was measured using a local region of interest centered on each tracked FA and

corrected for local background. FA lifetime was defined as the time interval between the first and last frames in which an individual FA was tracked. To determine the peak frame while minimizing the influence of transient frame-to-frame intensity fluctuations, a three-frame median filter was applied to the background-subtracted GFP–paxillin intensity trace, and the peak frame was defined as the frame corresponding to the maximum of the filtered trace. The assembly phase was defined as the increase in GFP–paxillin fluorescence intensity up to the peak frame, whereas the disassembly phase was defined as the decrease in fluorescence intensity from the peak frame. Assembly and disassembly rates were calculated as the slopes obtained by linear regression of the respective phases using the original background-subtracted fluorescence intensities normalized to the intensity at the defined peak frame. The disassembly rate was expressed as the absolute value of the slope. FAs that could be continuously tracked over time were included in the analysis. The same selection criteria were applied to control and KO-1 cells. A total of 40 FAs were analyzed in each independent experiment (n=5 independent experiments per group). FA lifetime was determined for all tracked FAs, whereas assembly and disassembly rates were calculated only for FAs in which the respective phases could be identified. The mean value for each parameter in each independent experiment was used as one biological replicate.

3D-STED super-resolution microscopy

Cell fixation and blocking were performed as described above. The cells were subsequently incubated with an anti-GFP antibody (MBL) diluted in Can Get Signal Solution 1 (TOYOBO) overnight at 4°C. A goat anti-rabbit IgG antibody conjugated to Alexa Fluor 594 (Invitrogen) was used to label the primary antibodies. Phalloidin-Star-Red (Abberior) was used for the labeling of F-actin. Cells were transferred onto slides and mounted with ProLong Glass Antifade Mountant (Thermo Fisher Scientific). 3D-STED super-resolution images were acquired on an Expert Line STED microscope (Abberior Instruments) coupled to an inverted IX83 platform (Olympus). A 100× oil objective (NA=1.4, Olympus) was used for all the measurements, and the confocal pinhole was set to 0.9 Airy units. Alexa Fluor 594 and Star-Red were excited with pulsed 561 nm and 640 nm lasers, respectively, whereas a 775 nm beam served as the depletion laser. Data were collected in 3D-STED mode at 50 nm/pixel, and fluorescence was detected with an avalanche photodiode.

Electron microscopy analysis

MTD-1A cells were cultured on gridded polymer-bottom dishes (µ-Dish 35 mm, high Grid-500; ibidi, Martinsried, Germany). After various experimental treatments, the cells were fixed with 2% formaldehyde and 2.5% glutaraldehyde in 0.1 M cacodylate buffer (pH 7.4) at room temperature for 2 h. During fixation, the positions of the cells of interest, together with their fluorescence images, were recorded using an A1 confocal laser scanning microscope (Nikon). After five washes with 0.1 M cacodylate buffer, the cells were postfixed with 1.5% potassium ferrocyanide and 2% osmium tetroxide in the same buffer at 4°C for 1 h, followed by five washes with Milli-Q water. The cells were then incubated in 0.5% uranyl acetate in Milli-Q water at room temperature for 2 h and washed five times with Milli-Q water. The cells were dehydrated through a graded ethanol series (30, 65, 80, 90, 95 and 99.5% for 10 min each, followed by three changes of 100% ethanol for 20 min each) and subsequently infiltrated with Epon 812 resin (TAAB). Polymerization was carried out at 65°C for 72 h. To remove the polymer coverslip, the resin blocks in plastic dishes were immersed in toluene. The grid pattern of the coverslip was clearly transferred onto the surface of the resin.

Ultrathin sections (70 nm) were cut using a diamond knife on an ultramicrotome (Leica EM UC7; Leica Microsystems, Wetzlar, Germany) and collected on silicon wafers. The sections were conventionally double-stained with uranyl acetate and lead nitrate. Observations were performed using a field-emission scanning electron microscope (JSM-IT800SHL; JEOL, Tokyo, Japan) at 3 kV with a backscattered electron detector.

Cells of interest were identified in electron microscopy images based on morphological information from bright-field and fluorescence images acquired on gridded coverslips by confocal microscopy.

RNA sequencing and gene expression analysis

RNA-seq libraries were prepared using the TruSeq Stranded mRNA Library Preparation Kit (Illumina). Paired-end sequencing (2x 101 bp) was performed on the Illumina NovaSeq 6000 platform. FASTQ files were subsequently mapped and aligned to the mouse mm10 reference genome based on Ensembl annotations using the built-in RNA-seq analysis module in CLC Genomics Workbench (Qiagen) with default settings. To quantify gene expression levels, transcripts per million (TPM) and reads per kilobase of transcript per million mapped reads (RPKM) values were calculated for each gene.

Purification of recombinant proteins from HEK293 cells

HEK293 cells were seeded at a density of 1.5×10^6 cells on 100-mm dishes and transfected the following day with 12 µg of each plasmid using PEI-Max transfection reagent. After a 48-h incubation at 37°C, the cells were washed once and scraped from the dishes in PBS. For His–GFP–JRAB, the cells collected from 60 dishes were lysed in 300 µl of buffer A [10 mM Tris-HCl pH 8.0, 1 mM EDTA, 1% (w/v) Nonidet P-40, 150 mM NaCl and 10 µM p-APMSF], and then the cell lysates were centrifuged at 4°C for 5 min at 16,100 ***g***. The supernatants collected from 30 dishes were applied to a cOmplete resin column (Roche). The pass-through fraction was applied to the same column a second time. The column was subsequently washed with buffer B (50 mM Tris-HCl at pH 7.5, 150 mM NaCl, 2 mM DTT, and 10 mM imidazole). The proteins remaining in the column were eluted with buffer C (50 mM Tris-HCl pH 7.5, 150 mM NaCl, 2 mM DTT and 100 mM imidazole) and subjected to SDS-PAGE. The samples were concentrated, and then 500 µl of the protein solution was applied to a Superdex 200 PC 3.2/30 (GE Healthcare) column (2.6 cm×6.6 cm) equilibrated with buffer D (25 mM Tris-HCl pH 7.5, 0.5 mM EDTA, 1 mM DTT and 150 mM NaCl). Elution was performed with buffer D at a flow rate of 250 µl/min. Fractions were collected and subjected to SDS-PAGE, followed by Coomassie Brilliant Blue staining. For His–mCherry–Rab13DA, cells collected from 60 dishes were sonicated in 25 ml of buffer E (20 mM Tris-HCl pH 8.0, 5 mM $MgCl_2$, 100 mM NaCl and 10 µM p-APMSF), after which the homogenates were centrifuged at 4°C for 1 h at 100,000 ***g***. The pellet fractions were extracted with buffer F (20 mM Tris-HCl pH 8.0, 5 mM $MgCl_2$, 100 mM NaCl, 1% CHAPS and 10 µM p-APMSF) and centrifuged at 4°C for 1 h at 100,000 ***g***. The supernatants (extracted fractions) were applied to a Talon resin column (Contech). The pass-through fraction was applied to the same column a second time. The column was subsequently washed with buffer G (20 mM Tris-HCl pH 8.0, 5 mM $MgCl_2$, 100 mM NaCl, 0.6% CHAPS and 10 mM imidazole). The proteins remaining in the column were eluted with buffer H (20 mM Tris-HCl pH 8.0, 5 mM $MgCl_2$, 100 mM NaCl, 0.6% CHAPS, and 100 mM imidazole) and subjected to SDS-PAGE.

Fluorescence-labeled F-actin preparation

F-actin was prepared according to the manufacturer's instructions (Cytoskeleton, Inc.). Briefly, first, G-actin (AKL99; Cytoskeleton, Inc.) was resuspended at 1 mg/ml in general actin buffer (5 mM Tris-HCl pH 8, 0.2 mM $CaCl_2$, 0.2 mM ATP and 0.5 mM DTT) and left on ice for 30 min. Then, G-actin was polymerized by the addition of 10× actin polymerization buffer (500 mM KCl, 20 mM $MgCl_2$ and 10 mM ATP) (1× final concentration), after which the mixture was incubated at room temperature for 1 h (23 µM stock). Finally, F-actin was diluted from 23 µM to 5 µM and mixed with Alexa Fluor 647-labeled phalloidin (Invitrogen) to obtain a final concentration of 3 µM fluorescence-labeled F-actin.

Formation of phase-separated droplets with crowding agents

To observe the droplets, 25% PEG (final concentration: 4.3–5%; Wako #169-09125) was added to a mixture of purified His–GFP–JRAB with or without His–mCherry–Rab13DA. The mixture was placed on a glass-bottom dish. Images were acquired using an A1 confocal laser scanning microscope (Nikon) equipped with an oil objective lens (PlanApo VC60×, NA=1.4).

In vitro F-actin bundling experiments

To observe the formation of F-actin bundles, fluorescently labeled F-actin was added to various droplets placed on a glass-bottom dish, covered to

avoid evaporation, and observed using an A1 confocal laser scanning microscope (Nikon) equipped with an oil objective lens (PlanApo VC 60×, NA=1.4) or an N-SIM super-resolution microscope (Nikon) equipped with a comparable water-immersion objective lens. The images shown are representative of at least three independent experiments.

High-speed atomic force microscopy

High-speed atomic force microscopy (Ando et al., 2001) was recently extended to the use of the measurement of mechanical properties. This extension is known as high-speed in-line force mapping (HS-iFM) (Ganser et al., 2025). In this study, we used HS-iFM to measure the mechanical properties of LLPS droplets. The HS-AFM used was a laboratory-built tip-scanning HS-AFM combined with a fluorescence microscope (Fukuda et al., 2013). The cantilevers were Olympus AC10 cantilevers with an electron-deposited carbon tip with a typical tip radius of 5 nm. The spring constant was calibrated using the thermal noise method (Hutter and Bechhoefer, 1993). The detailed calibration procedure is described in (Ganser et al., 2025) and revealed the spring constant to be 0.20±0.07 N/m. The resonance frequency was 444±100 kHz, and the Q factor was 1.46±0.2. These values are averages (mean±s.d.) of six measurements.

The topography scan time was set to 5 s, and the force map resolution was 50×50 pixels, with a loading time of 500 µs and a 300 nm extension, leading to a loading rate of 600 µm/s. The total imaging time was 15 s/frame. For each droplet, 2 to 11 frames were recorded. The elastic modulus of a droplet was averaged from an area of at least 100 pixels, close to the center of the droplet. Elastic modulus values were determined by fitting the force curve with the Hertz model (Hertz, 1882; Popov et al., 2019), as no significant adhesion force was present.

GFP–JRAB droplets were formed by mixing 3 µl of GFP–JRAB (20 µM) with 7 µl of buffer D and 10 µl of buffer H and adding 5 µl of PEG (25%) to a final concentration of 5%. After pipetting, the mixture was incubated at room temperature for 20 min. GFP–JRAB+mCherry–Rab13DA droplets were subjected to the same procedure, except that the components mixed together were 3 µl of GFP–JRAB (20 µM), 3 µl of mCherry–Rab13DA (20 µM), 7 µl of buffer D and 7 µl of buffer H. The HS-iFM measurements were carried out immediately after the droplets were formed.

To perform the HS-iFM measurements, the droplets were immobilized on a cover glass (Matsunami NEO, Matsunami, Japan). The glass was rinsed with water to remove dust. First, 20 µl of buffer D was added, after which 5 µl of the droplet suspension was added and incubated for 10 min. Afterward, the unattached droplets were washed off by rinsing with 200 µl of buffer D.

FRAP method

FRAP measurements were performed using a Leica TCS SP8 STED 3X FALCON microscope. The microscope is equipped with a white light laser (WLL), which was operated at 488 nm wavelength for imaging GFP–JRAB. FRAP works by first imaging the sample to obtain a baseline, then a selected area will be photobleached, after which imaging continues. From the recovery of the fluorescence signal, the mobile fraction can be calculated.

For imaging – before and after photobleaching – the intensity of the laser was adjusted depending on the sample to limit unwanted photobleaching while maintaining a sufficient contrast. For droplets of GFP–JRAB, the laser was set to 0.2% intensity, for GFP–JRAB+mCherry–Rab13DA the intensity was between 0.4% and 0.8%, and for imaging GFP–JRAB–F-actin bundles, the intensity was set to 5% of the maximum intensity. Images were recorded at 80 ms per frame. 50 frames were recorded before photobleaching, and after photobleaching 500 frames were recorded. For photobleaching, the intensity was increased to 50% for all samples, and a single spot was irradiated for 10 ms. This led to a circular bleached area (diameter of ∼600 nm). The intensity of the bleached area was typically ∼50% of the initial intensity just after bleaching. The FRAP curves were normalized regarding an unbleached area as well as regarding the intensity just before bleaching (Muzzopappa et al., 2022). This leads to curves that can assume values between 0 and 1, where 0 would be no recovery and 1 would be full recovery. The mobile fraction is the value of the normalized recovery curve after a plateau was reached. For the purpose of comparing the samples, the last ten datapoints of the recovery curve for each experiment were defined as the mobile fraction. Note that from the average recovery curves (Fig. S14) GFP–JRAB and GFP–JRAB+mCherry–Rab13DA seem to reach a plateau, whereas GFP–JRAB–F-actin has a lingering slope, even after ∼40 s of recovery, indicating that recovery is still continuing. Statistical analysis was performed using unpaired two-tailed Welch's *t*-tests (Welch, 1947). The three pairwise comparisons shown in Fig. 7C were pre-planned and were not corrected for multiple comparisons.

Use of AI tools

ChatGPT (OpenAI) was used with human oversight to assist with the visualization of author-provided numerical data and the preparation of graphs. All graphical outputs were reviewed and verified against the original data by the authors.

Acknowledgements

We thank Sawako Mima (our laboratory) and Shigehiro Shimazu (Nikon Solutions Co., Ltd.) for technical assistance. This work was supported by COI-NEXT Support Unit for Imaging Science at Kento.

Competing interests

The authors declare no competing or financial interests.

Author contributions

Conceptualization: A.S., T.S.; Data curation: A.S.; Formal analysis: C.G., Y.M., T.K., T.U., K.H.; Investigation: A.S., C.G., K.H., C.S., M.S., M.O., N.O., N.M., H.Y., K.T., K.M., K.K., H.K., S.Y., T.U., T.S.; Validation: A.S., C.G., Y.M., T.K.; Writing – original draft: A.S., C.G., K.H., N.M., H.K., S.Y., T.U., T.S.; Writing – review & editing: A.S., T.S.

Funding

This work was mainly supported by Japan Society for the Promotion of Science (JSPS) KAKENHI Grant Numbers JP 21K06838 (A.S.), JP 24K01309, JP 26H01626 (T.U.) and the Ministry of Education, Culture, Sports, Science and Technology (MEXT) Promotion of Development of a Joint Usage/Research System Project: Coalition of Universities for Research Excellence Program (CURE) (Grant Number JPMXP1323015482); the project budget of the National Institutes of Biomedical Innovation, Health and Nutrition (NIBN) (T.K.); Takeda Science Foundation (A.S.); Osaka Foundation for Promotion of Fundamental Medical Research (A.S.); and the Research Cluster program of the Tokushima University (T.S., A.S.; organizer, Y. Nishioka). This work was also supported by the Japan Society for the Promotion of Science Program for Forming Japan's Peak Research Universities (J-PEAKS), Grant Number JPJS 00420240022. This research was supported by Joint Research of the Exploratory Research Center on Life and Living Systems (ExCELLS; ExCELLS program No. 22EXC346). Open Access funding provided by Tokushima University. Deposited in PMC for immediate release.

First Person

This article has an associated First Person interview with the first author of the paper.

Data and resource availability

The RNA-seq data have been deposited in the DDBJ BioProject database under accession number PRJDB40037. All other data supporting this study are available from the corresponding author upon reasonable request. All relevant data and details of resources can be found within the article and its supplementary information.

References

Ando, T., Kodera, N., Takai, E., Maruyama, D., Saito, K. and Toda, A. (2001). A high-speed atomic force microscope for studying biological macromolecules. *Proc. Natl. Acad. Sci. USA* **98**, 12468-12472. doi:10.1073/pnas.211400898

Balaban, N. Q., Schwarz, U. S., Riveline, D., Goichberg, P., Tzur, G., Sabanay, I., Mahalu, D., Safran, S., Bershadsky, A., Addadi, L. et al. (2001). Force and focal adhesion assembly: a close relationship studied using elastic micropatterned substrates. *Nat. Cell Biol.* **3**, 466-472. doi:10.1038/35074532

Beutel, O., Maraspini, R., Pombo-García, K., Martin-Lemaitre, C. and Honigmann, A. (2019). Phase separation of zonula occludens proteins drives formation of tight junctions. *Cell* **179**, 923-936.e11. doi:10.1016/j.cell.2019.10.011

Cong, L., Ran, F. A., Cox, D., Lin, S., Barretto, R., Habib, N., Hsu, P. D., Wu, X., Jiang, W., Marraffini, L. A. et al. (2013). Multiplex genome engineering

using CRISPR/Cas systems. *Science* **339**, 819-823. doi:10.1126/science.1231143

Fujioka, Y., Alam, J. M., Noshiro, D., Mouri, K., Ando, T., Okada, Y., May, A. I., Knorr, R. L., Suzuki, K., Ohsumi, Y. et al. (2020). Phase separation organizes the site of autophagosome formation. *Nature* **578**, 301-305. doi:10.1038/s41586-020-1977-6

Fukuda, S., Uchihashi, T., Iino, R., Okazaki, Y., Yoshida, M., Igarashi, K. and Ando, T. (2013). High-speed atomic force microscope combined with single-molecule fluorescence microscope. *Rev. Sci. Instrum.* **84**, 073706. doi:10.1063/1.4813280

Furuse, M. and Tsukita, S. (2006). Claudins in occluding junctions of humans and flies. *Trends Cell Biol.* **16**, 181-188. doi:10.1016/j.tcb.2006.02.006

Ganser, C., Nishiguchi, S., Chan, F.-Y. and Uchihashi, T. (2025). A look beyond topography: Transient phenomena of Escherichia coli cell division captured with high-speed in-line force mapping. *Sci. Adv.* **11**, eads3010. doi:10.1126/sciadv.ads3010

Giridharan, S. S. P. and Caplan, S. (2014). MICAL-family proteins: complex regulators of the actin cytoskeleton. *Antioxid. Redox Signal.* **20**, 2059-2073. doi:10.1089/ars.2013.5487

Giridharan, S. S. P., Rohn, J. L., Naslavsky, N. and Caplan, S. (2012). Differential regulation of actin microfilaments by human MICAL proteins. *J. Cell Sci.* **125**, 614-624. doi:10.1242/jcs.089367

Grosshans, B. L., Ortiz, D. and Novick, P. (2006). Rabs and their effectors: achieving specificity in membrane traffic. *Proc. Natl. Acad. Sci. USA* **103**, 11821-11827. doi:10.1073/pnas.0601617103

Hartsock, A. and Nelson, W. J. (2008). Adherens and tight junctions: structure, function and connections to the actin cytoskeleton. *Biochim. Biophys. Acta* **1778**, 660-669. doi:10.1016/j.bbamem.2007.07.012

Hertz, H. (1882). Ueber die Berührung fester elastischer Körper. *Journal für die reine und angewandte Mathematik* 1882, 156-171. doi:10.1515/crll.1882.92.156

Huber, L. A., Pimplikar, S. W., Parton, R. G., Virta, H., Zerial, M. and Simons, K. (1993). Rab8, a small GTPase involved in vesicular traffic between the TGN and the basolateral plasma membrane. *J. Cell Biol.* **123**, 35-45. doi:10.1083/jcb.123.1.35

Hung, R.-J., Pak, C. W. and Terman, J. R. (2011). Direct redox regulation of F-actin assembly and disassembly by Mical. *Science* **334**, 1710-1713. doi:10.1126/science.1211956

Hutagalung, A. H. and Novick, P. J. (2011). Role of Rab GTPases in membrane traffic and cell physiology. *Physiol. Rev.* **91**, 119-149. doi:10.1152/physrev.00059.2009

Hutin, S., Kumita, J. R., Strotmann, V. I., Dolata, A., Ling, W. L., Louafi, N., Popov, A., Milhiet, P.-E., Blackledge, M., Nanao, M. H. et al. (2023). Phase separation and molecular ordering of the prion-like domain of the Arabidopsis thermosensory protein EARLY FLOWERING 3. *Proc. Natl. Acad. Sci. USA* **120**, e2304714120. doi:10.1073/pnas.2304714120

Hutter, J. L. and Bechhoefer, J. (1993). Calibration of atomic-force microscope tips. *Rev. Sci. Instrum.* **64**, 1868-1873. doi:10.1063/1.1143970

Itoh, M., Furuse, M., Morita, K., Kubota, K., Saitou, M. and Tsukita, S. (1999). Direct binding of three tight junction-associated MAGUKs, ZO-1, ZO-2, and ZO-3, with the COOH termini of claudins. *J. Cell Biol.* **147**, 1351-1363. doi:10.1083/jcb.147.6.1351

Jawerth, L., Fischer-Friedrich, E., Saha, S., Wang, J., Franzmann, T., Zhang, X., Sachweh, J., Ruer, M., Ijavi, M., Saha, S. et al. (2020). Protein condensates as aging Maxwell fluids. *Science* **370**, 1317-1323. doi:10.1126/science.aaw4951

Köhler, K., Louvard, D. and Zahraoui, A. (2004). Rab13 regulates PKA signaling during tight junction assembly. *J. Cell Biol.* **165**, 175-180. doi:10.1083/jcb.200312118

Kroschwald, S., Maharana, S. and Simon, A. (2017). Hexanediol: a chemical probe to investigate the material properties of membrane-less compartments. *Matters*. 10.19185/matters.201702000010.

Marzesco, A. M., Dunia, I., Pandjaitan, R., Recouvreur, M., Dauzonne, D., Benedetti, E. L., Louvard, D. and Zahraoui, A. (2002). The small GTPase Rab13 regulates assembly of functional tight junctions in epithelial cells. *Mol. Biol. Cell.* **13**, 1819-1831. doi:10.1091/mbc.02-02-0029

Miyake, K., Sakane, A., Tsuchiya, Y., Sagawa, I., Tomida, Y., Kasahara, J., Imoto, I., Watanabe, S., Higo, D., Mizuguchi, K. et al. (2019). Actin cytoskeletal reorganization function of JRAB/MICAL-L2 is fine-tuned by intramolecular interaction between first LIM zinc finger and C-terminal coiled-coil domains. *Sci. Rep.* **9**, 12794. doi:10.1038/s41598-019-49232-8

Muzzopappa, F., Hummert, J., Anfossi, M., Tashev, S. A., Herten, D.-P. and Erdel, F. (2022). Detecting and quantifying liquid–liquid phase separation in living cells by model-free calibrated half-bleaching. *Nat. Commun.* **13**, 7787. doi:10.1038/s41467-022-35430-y

Nakatsuji, H., Nishimura, N., Yamamura, R., Kanayama, H. and Sasaki, T. (2008). Involvement of Actinin-4 in the recruitment of JRAB/MICAL-L2 to cell-cell junctions and the formation of functional tight junctions. *Mol. Cell. Biol.* **28**, 3324-3335. doi:10.1128/MCB.00144-08

Pasapera, A. M., Schneider, I. C., Rericha, E., Schlaepfer, D. D. and Waterman, C. M. (2010). Myosin II activity regulates vinculin recruitment to focal adhesions through FAK-mediated paxillin phosphorylation. *J. Cell Biol.* **188**, 877-890. doi:10.1083/jcb.200906012

Peränen, J. (2011). Rab8 GTPase as a regulator of cell shape. *Cytoskeleton* **68**, 527-539. doi:10.1002/cm.20529

Philippe, S., Sarkis, C., Barkats, M., Mammeri, H., Ladroue, C., Petit, C., Mallet, J. and Serguera, C. (2006). Lentiviral vectors with a defective integrase allow efficient and sustained transgene expression in vitro and in vivo. *Proc. Natl. Acad. Sci. USA* **103**, 17684-17689. doi:10.1073/pnas.0606197103

Pokutta, S. and Weis, W. I. (2002). The cytoplasmic face of cell contact sites. *Curr. Opin. Struct. Biol.* **12**, 255-262. doi:10.1016/S0959-440X(02)00318-4

Pombo-García, K., Adame-Arana, O., Martin-Lemaitre, C., Jülicher, F. and Honigmann, A. (2024). Membrane prewetting by condensates promotes tight-junction belt formation. *Nature* **632**, 647-655. doi:10.1038/s41586-024-07726-0

Popov, V. L., Heß, M. and Willert, E. (2019). *Handbook of contact mechanics: Exact solutions of axisymmetric contact problems*. Springer Berlin, Heidelberg. doi:10.1007/978-3-662-58709-6

Rubinstein, M. and Semenov, A. N. (1998). Thermoreversible gelation in solutions of associating polymers. 2. Linear dynamics. *Macromolecules* **31**, 1386-1397. doi:10.1021/ma970617

Sakane, A. and Sasaki, T. (2015). Roles of Rab family small G proteins in formation of the apical junctional complex in epithelial cells. In *Cell Polarity*, Vol. 1 (ed. K. Ebnet), pp. 349-374. Cham: Springer International Publishing.

Sakane, A., Abdallah, A. A. M., Nakano, K., Honda, K., Ikeda, W., Nishikawa, Y., Matsumoto, M., Matsushita, N., Kitamura, T. and Sasaki, T. (2012). Rab13 small G protein and junctional Rab13-binding protein (JRAB) orchestrate actin cytoskeletal organization during epithelial junctional development. *J. Biol. Chem.* **287**, 42455-42468. doi:10.1074/jbc.M112.383653

Sakane, A., Abdallah, A. A. M., Nakano, K., Honda, K., Kitamura, T., Imoto, I., Matsushita, N. and Sasaki, T. (2013). Junctional Rab13-binding protein (JRAB) regulates cell spreading via filamins. *Genes Cells* **18**, 810-822. doi:10.1111/gtc.12078

Sakane, A., Yoshizawa, S., Nishimura, M., Tsuchiya, Y., Matsushita, N., Miyake, K., Horikawa, K., Imoto, I., Mizuguchi, C., Saito, H. et al. (2016). Conformational plasticity of JRAB/MICAL-L2 provides “law and order” in collective cell migration. *Mol. Biol. Cell* **27**, 3095-3108. doi:10.1091/mbc.e16-05-0332

Sakane, A., Yano, T.-A., Uchihashi, T., Horikawa, K., Hara, Y., Imoto, I., Kurisu, S., Yamada, H., Takei, K. and Sasaki, T. (2021). JRAB/MICAL-L2 undergoes liquid-liquid phase separation to form tubular recycling endosomes. *Commun. Biol.* **4**, 551. doi:10.1038/s42003-021-02080-7

Sawa-Makarska, J., Baumann, V., Coudevylle, N., von Bülow, S., Nogellova, V., Abert, C., Schuschnig, M., Graef, M., Hummer, G. and Martens, S. (2020). Reconstitution of autophagosome nucleation defines Atg9 vesicles as seeds for membrane formation. *Science* **369**, eaaz7714. doi:10.1126/science.aaz7714

Schwayer, C., Shamipour, S., Pranjic-Ferscha, K., Schauer, A., Balda, M., Tada, M., Matter, K. and Heisenberg, C.-P. (2019). Mechanosensation of tight junctions depends on ZO-1 phase separation and flow. *Cell* **179**, 937-952.e18. doi:10.1016/j.cell.2019.10.006

Spector, I., Shochet, N. R., Kashman, Y. and Groweiss, A. (1983). Latrunculins: novel marine toxins that disrupt microfilament organization in cultured cells. *Science* **219**, 493-495. doi:10.1126/science.6681676

Stenmark, H. (2009). Rab GTPases as coordinators of vesicle traffic. *Nat. Rev. Mol. Cell Biol.* **10**, 513-525. doi:10.1038/nrm2728

Stevenson, B. R., Siliciano, J. D., Mooseker, M. S. and Goodenough, D. A. (1986). Identification of ZO-1: a high molecular weight polypeptide associated with the tight junction (zonula occludens) in a variety of epithelia. *J. Cell Biol.* **103**, 755-766. doi:10.1083/jcb.103.3.755

Sun, D., Zhao, X., Wiegand, T., Martin-Lemaitre, C., Borianne, T., Kleinschmidt, L., Grill, S. W., Hyman, A. A., Weber, C. and Honigmann, A. (2025). Assembly of tight junction belts by ZO1 surface condensation and local actin polymerization. *Dev. Cell* **60**, 1234-1250.e6. doi:10.1016/j.devcel.2024.12.012

Tang, J. X. and Janmey, P. A. (1996). The polyelectrolyte nature of F-actin and the mechanism of actin bundle formation. *J. Biol. Chem.* **271**, 8556-8563. doi:10.1074/jbc.271.15.8556

Terai, T., Nishimura, N., Kanda, I., Yasui, N. and Sasaki, T. (2006). JRAB/MICAL-L2 Is a Junctional Rab13-binding Protein Mediating the Endocytic Recycling of Occludin. *Mol. Biol. Cell* **17**, 2465-2475. doi:10.1091/mbc.e05-09-0826

Tsukita, S., Furuse, M. and Itoh, M. (2001). Multifunctional strands in tight junctions. *Nat. Rev. Mol. Cell Biol.* **2**, 285-293. doi:10.1038/35067088

Tsukita, S., Tanaka, H. and Tamura, A. (2019). The Claudins: from tight junctions to biological systems. *Trends Biochem. Sci.* **44**, 141-152. doi:10.1016/j.tibs.2018.09.008

Wandinger-Ness, A. and Zerial, M. (2014). Rab proteins and the compartmentalization of the endosomal system. *Cold Spring Harb. Perspect. Biol.* **6**, a022616. doi:10.1101/cshperspect.a022616

Wang, J., Choi, J.-M., Holehouse, A. S., Lee, H. O., Zhang, X., Jahnel, M., Maharana, S., Lemaitre, R., Pozniakovsky, A., Drechsel, D. et al. (2018). A molecular grammar governing the driving forces for phase separation of prion-like RNA binding proteins. *Cell* **174**, 688-699.e16. doi:10.1016/j.cell.2018.06.006

Wanisch, K. and Yáñez-Muñoz, R. J. (2009). Integration-deficient lentiviral vectors: a slow coming of age. *Mol. Ther.* **17**, 1316-1332. doi:10.1038/mt.2009.122

Welch, B. L. (1947). The generalisation of student's problems when several different population variances are involved. *Biometrika* **34**, 28-35. doi:10.1093/biomet/34.1-2.28

Yamamura, R., Nishimura, N., Nakatsuji, H., Arase, S. and Sasaki, T. (2008). The interaction of JRAB/MICAL-L2 with Rab8 and Rab13 coordinates the assembly of tight junctions and adherens junctions. *Mol. Biol. Cell* **19**, 971-983. doi:10.1091/mbc.e07-06-0551

Zaidel-Bar, R., Ballestrem, C., Kam, Z. and Geiger, B. (2003). Early molecular events in the assembly of matrix adhesions at the leading edge of migrating cells. *J. Cell Sci.* **116**, 4605-4613. doi:10.1242/jcs.00792

Zerial, M. and McBride, H. (2001). Rab proteins as membrane organizers. *Nat. Rev. Mol. Cell Biol.* **2**, 107-117. doi:10.1038/35052055

Zhen, Y. and Stenmark, H. (2015). Cellular functions of Rab GTPases at a glance. *J. Cell Sci.* **128**, 3171-3176. doi:10.1242/jcs.166074

Zucchini, D., Caprini, G., Pasterkamp, R. J., Tedeschi, G. and Vanoni, M. A. (2011). Kinetic and spectroscopic characterization of the putative monooxygenase domain of human MICAL-1. *Arch. Biochem. Biophys.* **515**, 1-13. doi:10.1016/j.abb.2011.08.004